



**HAL**  
open science

## Seasonal patterns in greenhouse gas emissions from lakes and ponds in a High Arctic polygonal landscape

Vilmantas Prėskienis, Isabelle Laurion, Frédéric Bouchard, Peter Douglas, Michael Billett, Daniel Fortier, Xiaomei Xu

### ► To cite this version:

Vilmantas Prėskienis, Isabelle Laurion, Frédéric Bouchard, Peter Douglas, Michael Billett, et al.. Seasonal patterns in greenhouse gas emissions from lakes and ponds in a High Arctic polygonal landscape. *Limnology and Oceanography*, 2021, 66 (S1), pp.S117-S141. 10.1002/lno.11660 . hal-04505252

**HAL Id: hal-04505252**

**<https://hal.science/hal-04505252v1>**

Submitted on 19 Sep 2024

**HAL** is a multi-disciplinary open access archive for the deposit and dissemination of scientific research documents, whether they are published or not. The documents may come from teaching and research institutions in France or abroad, or from public or private research centers.

L'archive ouverte pluridisciplinaire **HAL**, est destinée au dépôt et à la diffusion de documents scientifiques de niveau recherche, publiés ou non, émanant des établissements d'enseignement et de recherche français ou étrangers, des laboratoires publics ou privés.



Distributed under a Creative Commons Attribution 4.0 International License

## Seasonal patterns in greenhouse gas emissions from lakes and ponds in a High Arctic polygonal landscape

Vilmantas Prėskienis <sup>1,2\*</sup> Isabelle Laurion <sup>1,2</sup> Frédéric Bouchard <sup>1,2,3</sup> Peter M. J. Douglas,<sup>4</sup> Michael F. Billett,<sup>5</sup> Daniel Fortier,<sup>2,6</sup> Xiaomei Xu<sup>7</sup>

<sup>1</sup>Centre Eau Terre Environnement, Institut national de la recherche scientifique, Québec, Canada

<sup>2</sup>Centre d'études nordiques (CEN), Université Laval, Québec, Canada

<sup>3</sup>Géosciences Paris-Saclay (GEOPS), Université Paris-Saclay, Orsay, France

<sup>4</sup>Department of Earth and Planetary Sciences and Geotop, McGill University, Montréal, Canada

<sup>5</sup>Biological and Environmental Sciences, Faculty of Natural Sciences, University of Stirling, Stirling, UK

<sup>6</sup>Département de Géographie, Université de Montréal, Montréal, Canada

<sup>7</sup>Department of Earth System Science, University of California, Irvine

### Abstract

Lakes and ponds can be hotspots for CO<sub>2</sub> and CH<sub>4</sub> emissions, but Arctic studies remain scarce. Here we present diffusive and ebullition fluxes collected over several years from 30 ponds and 4 lakes formed on an organic-rich polygonal tundra landscape. Water body morphology strongly affects the mixing regime—and thus the seasonal patterns in gas emissions—with ice-out and autumnal turnover periods identified as hot moments in most cases. The studied thermokarst lake maintained relatively high ebullition rates of millennia-old CH<sub>4</sub> (up to 3405 <sup>14</sup>C YBP). Larger and deeper kettle lakes maintained low fluxes of both gases (century to millennium-old), slowly turning into a CO<sub>2</sub> sink over the summer. During winter, lakes accumulated CO<sub>2</sub>, which was emitted during the ice-out period. Coalescent polygonal ponds, influenced by photosynthesizing benthic mats, were continuous CO<sub>2</sub> sinks, yet important CH<sub>4</sub> emitters (modern carbon). The highest fluxes were recorded from ice-wedge trough ponds (up to 96 mmol CO<sub>2</sub> equivalent m<sup>-2</sup> d<sup>-1</sup>). However, despite clear signs of permafrost carbon inputs via active shore erosion, these sheltered ponds emitted modern to century-old greenhouse gases. As the ice-free period lengthens, scenarios of warmer and wetter conditions could favor both the production of CO<sub>2</sub> and CH<sub>4</sub> from thawing permafrost carbon, and CH<sub>4</sub> production from recently fixed carbon through an atmospheric CO<sub>2</sub>-to-CH<sub>4</sub> shunt at sites in which primary production is stimulated. This must be carefully considered at the landscape scale, recognizing that older carbon stocks can be mineralized efficiently in specific locations, such as in thermokarst lakes.

High Arctic regions are experiencing pronounced climate change (Bintanja and Kriken 2016), affecting air and permafrost temperatures (Biskaborn 2019), and snowfall (Bokhorst 2016). Lowlands are widespread in this part of the world, and known for abundance (up to 90% of surface area in

certain regions; Pienitz et al. 2008) and diversity of water bodies. Lakes located in organic-rich permafrost substrate can be sites of intense carbon dioxide (CO<sub>2</sub>) and methane (CH<sub>4</sub>) emissions to the atmosphere (Abnizova et al. 2012; Sepulveda-Jauregui et al. 2015; Matveev et al. 2016). Small ponds have been identified as hot spots of biogeochemical activity (Holgerson and Raymond 2016), and this holds true for tundra ponds (Bouchard et al. 2015). Recent field and modeling studies showed that CO<sub>2</sub> and CH<sub>4</sub> emissions from Arctic lakes are significant and could increase with global warming (Kosten et al. 2010; Tan and Zhuang 2015; Wik et al. 2016a; Tan et al. 2017).

The carbon-based greenhouse gases (GHG; CO<sub>2</sub> and CH<sub>4</sub>) produced from old carbon pools mobilized through permafrost thawing could act as a positive feedback on climate warming (Schuur et al. 2015), although the magnitude of this mechanism remains largely unknown (reviewed by Dean

\*Correspondence: isabelle.laurion@ete.inrs.ca

Additional Supporting Information may be found in the online version of this article.

**Author Contribution Statement:** V.P., I.L., F.B., D.F., and M.B. have participated in study planning and data collection in the field. V.P. and I.L. performed the data analyses, with M.B., P.D., and X.X. adding their expertise in analyzing and interpreting the isotope data. V.P. wrote the manuscript under the supervision of I.L.. All authors have contributed to the writing or revision of the manuscript.

**Special Issue:** Biogeochemistry and Ecology across Arctic Aquatic Ecosystems in the Face of Change. Edited by: Peter J. Hernes, Suzanne E. Tank and Ronnie N. Glud

et al. 2018). The majority of organic-rich permafrost areas developed during the Holocene (Treat and Jones 2018), and in certain regions this led to the sequestration of large amounts of carbon (Hugelius 2014). The Holocene carbon storage may represent a feedback to climate change if recent permafrost erosion accelerates its transfer to the atmosphere, although most studies involving GHG dating up to now have taken place in yedoma regions (late Pleistocene deposits; e.g., Walter et al. 2008; Elder et al. 2019). Many recent studies have found that microorganisms predominantly mineralize freshly produced organic matter in high-latitude lakes (Bouchard et al. 2015; Elder et al. 2018; Bogard et al. 2019), except at sites strongly affected by deep permafrost thaw (Mann et al. 2015; Turetsky et al. 2020).

Studies presenting GHG fluxes from lakes and ponds of the Arctic tundra environment remain scarce, even though their importance was emphasized at least 30 years ago (Sebacher et al. 1986; Kling et al. 1992). To our knowledge, there are only six areas where GHG emissions from tundra lakes or wetlands have been studied: the Alaskan North Slope and Yukon Delta in the United States, the Lena Delta and Yamalia in the Russian Federation, and the Eastern Nunavut and Northwest Territories in Canada (Table 1). Furthermore, Arctic studies are often strongly limited temporally for logistical reasons, with only a few measurement points of the fluxes, most often restricted to July or August, or estimated from bubbles trapped in ice or from under-ice measurements (e.g., Langer et al. 2015; Matveev et al. 2019). Despite that, the few studies looking at spatiotemporal variations in CO<sub>2</sub> or CH<sub>4</sub> emissions

revealed strong seasonality, as well as dependence on the type of organic substrate (Sepulveda-Jauregui et al. 2015; Elder et al. 2018, 2019; Hughes-Allen et al. 2020), lake morphology (Abnizova et al. 2012), and lake–river connectivity (Cunada et al. 2018). Thus, more studies covering the whole open-water season and accounting for winter and summer storage fluxes (respectively, defined as the emission during the ice-out and autumnal mixing period of the GHG accumulated in the water column during preceding months) are needed to better assess the contribution of aquatic tundra ecosystems to the global carbon cycle, and their sensitivity to climate change.

Bylot Island is characterized by a Holocene organic-rich tundra landscape, where lake and pond limnology has been studied for over a decade, with initial CO<sub>2</sub> and CH<sub>4</sub> flux data presented in Breton et al. (2009) and Laurion et al. (2010), and later complemented with a few radiocarbon dates on samples collected in July (Negandhi et al. 2013; Bouchard et al. 2015). These studies showed high CO<sub>2</sub> and CH<sub>4</sub> emissions, primarily composed of modern carbon. Exploiting data collected from late May to mid-August, the present study aims to identify the key mechanisms behind the variability observed in CO<sub>2</sub> and CH<sub>4</sub> fluxes from lakes and ponds that characterize polygonal tundra landscapes. We investigated how water body morphology affects seasonal trends in fluxes of these gases through its influence on mixing regime, and which sources of carbon are predominantly mineralized in the water bodies by exploiting the gas isotopic signatures. This is particularly relevant since morphology can be recognized by spatially resolved remote

**Table 1.** Reported CO<sub>2</sub> and CH<sub>4</sub> fluxes from tundra lakes and ponds across the Arctic. Only studies on water bodies above the tree-line were selected. The ranges presented for Bylot Island are composed of averaged seasonal values from all studied water bodies, and include summer storage flux estimated from dissolved concentrations measured at the hypolimnion. Negative values represent CO<sub>2</sub> uptake from the atmosphere.

Region	References	Reported flux (mmol m <sup>-2</sup> d <sup>-1</sup> )			Notes*
		Diff CO <sub>2</sub>	Diff CH <sub>4</sub>	Ebul CH <sub>4</sub>	
Alaskan North Slope, United States	Elder et al. (2018)	0.2–82.0	0.16–0.56	n.a.	DG, HE; Apr, Aug
	Sepulveda-Jauregui et al. (2015)	6.7–50.3	0.46–1.63	0.20–4.5	HE, SR; Apr, Jun–Jul
	Kling et al. (1992)	–5.5 to 59.8	0.23–1.02	n.a.	DIC, HE; Jul
	Sebacher et al. (1986)	n.a.	2.1–16.6	n.a.	CH; Aug
Bylot Island, Canada	This study, Laurion et al. (2010), Negandhi et al. (2013), Bouchard et al. (2015)	–10.4 to 81.5	0.02–8.9	0.01–16.9	HE, SR, CH; Jun–Aug
Ellesmere Island, Canada	Emmerton et al. (2016)	–6.5 to 5.1	0.01–0.56	0.01–0.43	HE, SR, EC; Jun–Aug
Lena Delta, RF <sup>†</sup>	Abnizova et al. (2012)	9.0–25.9	n.a.	n.a.	EC; Aug–Sep
Northwestern Canadian Arctic	Cunada et al. (2018)	n.a.	0.12–57.0	n.a.	HE; May–Aug
	Buell (2015)	–0.08 to 3.9	n.a.	n.a.	CH, HE, SR; Jun–Aug
Yamalia, RF <sup>†</sup>	Golubyatnikov and Kazantsev (2013)	n.a.	0.36–0.79	n.a.	CH; Aug
Yukon Delta, USA	Bartlett et al. (1992)	n.a.	3.0–229.6	n.a.	CH; Jul

\*Methods for acquiring diffusive flux: CH, gas chamber; DG, degassing membrane contactor; DIC, obtained from dissolved inorganic carbon; EC, eddy covariance flux tower; HE, headspace equilibration; SR, sensors measuring concentration directly in the field. The months roughly indicate when field sampling was done.

<sup>†</sup>Russian Federation.

sensing tools (as in Elder et al. 2020), making such relationships informative for upscaling exercises.

## Methods

### Description of the study site

The study was conducted on Bylot Island, on the eastern side of the Canadian Arctic Archipelago, in Sirmilik National Park, Nunavut. The core of the island is composed of the Byam Martin Mountains, consisting of igneous and metamorphic rocks and covered by ice caps. The surrounding undulating lowlands, covered by graminoid-moss tundra (Duclos et al. 2006), are made up of poorly consolidated sedimentary rocks, where previous glaciations have carved a series of valleys, and left behind a cover of glacial sediments (Klassen 1993). All the lakes and ponds presented in this study are located in one of these valleys, named Qarlikturvik (glacier C-79; 73°09'N, 79°58'W), located on the western side of the island and dominated by a braided river fed by glacial meltwater. A 3 to 5-m thick syngenetic permafrost terrace, a mixture of windblown loess and peat, has been accumulating since the mid-Holocene (Fortier et al. 2006). These peaty loess deposits contain excess pore ice (> 100% dry weight) and their gravimetric organic matter content can reach more than 50%. The active layer depth in these deposits generally ranges from 40 to 60 cm (Fortier and Allard 2004). This continuous permafrost terrain is characterized by a complex network of ice-wedge polygons with well-defined ridges and troughs.

The region experiences a polar climate characterized by short cool summers, long cold winters, and low precipitation. The climate normal is based on 1981–2010 data provided by the Environment Canada meteorological station in Mittimatalik (Pond Inlet), located 85 km southeast of the study site. For this time period, mean annual air temperature was  $-14.6^{\circ}\text{C}$  and precipitation 189 mm (91 mm of rain) (Environment Canada, [https://climate.weather.gc.ca/climate\\_normals/index\\_e.html](https://climate.weather.gc.ca/climate_normals/index_e.html)). In recent decades, the climate in the Eastern Canadian Arctic has been experiencing one of the most rapid changes in the Arctic. The greatest warming trends are observed for autumn and winter seasons (with warming in some areas exceeding  $1.7^{\circ}\text{C}$  per decade) leading to shorter snow-covered periods, yet with increased total winter precipitation (Bell and Brown 2018).

During the thawing period, large portions of the valley retain snowmelt water in closed depressions, creating thousands of shallow (0.1–1.5 m depth) water bodies of diverse shapes and sizes (Fig. 1). These aquatic systems freeze completely during winter as the average maximum ice thickness at the study site is  $2\text{ m} \pm 20\text{ cm}$  (measured in 2015 and 2016), which makes their annual biogeochemical cycle very different from the larger and deeper lakes present in the valley. We used this distinction to define lakes (> 2 m depth) with a fraction of the water column remaining unfrozen in winter, and ponds (< 2 m depth) that freeze to the bottom. This

distinction is in agreement with other studies in the Arctic classifying lakes and ponds based on area (Langer et al. 2015; Polishchuk et al. 2018)—the majority of the ponds at our site are smaller than  $500\text{ m}^2$ , and all studied lakes are larger than  $10,000\text{ m}^2$ .

### Water body selection

In total, 30 ponds and 4 lakes were studied for their limnology, biogeochemistry, and fluxes of  $\text{CO}_2$  and  $\text{CH}_4$ . Some lakes and ponds have been sampled sporadically since 2008, but the majority of the data presented here is from four consecutive summers (2014–2017), in 2015 starting late May and in 2016 extending until mid-August. The chosen water bodies are well represented at the study site (Fig. 1).

Two of the chosen lakes (Table 2) were formed in kettle basins and are mainly surrounded by inorganic glaciofluvial deposits and till. This type of glacial lake is common across the Arctic (Wik et al. 2016a). Since they fill depressions left by melted glacial ice, they tend to be deeper (> 5 m) than other types of freshwater bodies in the area. The valley also contains several thermokarst lakes formed within the above-mentioned organic-rich peat-loess complex. Most of these lakes are shallow (< 3 m), which is typical for thermokarst lakes outside yedoma regions (Grosse et al. 2013). One of the chosen thermokarst lakes, BYL123, has an elongated shape (Fig. 1) and two deeper basins (2–2.5 m deep). Lake BYL66 is the largest and deepest thermokarst lake in the valley, presenting a large central zone with a bumpy bottom ( $\sim 4\text{ m}$  deep), and a wide shallow littoral zone (< 2 m deep) that continues to expand by thermokarst and thermo-erosional wave action (see Bouchard et al. 2020 for details on the bathymetry and temporal evolution of this lake).

The study ponds were chosen to represent the most frequent morphologies observed at the site (Table 2). They can be roughly divided into two categories: (1) narrow (0.5–5.0 m wide; 0.4–1.5 m deep), elongated, channel-like ponds formed above degrading ice wedges, hereafter referred to as ice wedge trough (IWT) ponds, and (2) wider ponds (5–35 m wide; 0.5–0.9 m deep) with steep shores and flat bottoms, often occupying several polygons, hereafter referred to as coalescent polygonal (CP) ponds. The IWT ponds have dark, humic, turbid waters, rich in allochthonous organic matter originating from shore erosion and linked to their large soil–water contact areas relative to their volume. In contrast, CP ponds are more transparent, warmer, and shallower, with a flat bottom covered by benthic mats mainly composed of cyanobacteria (*Oscillatoria* sp.; Vézina and Vincent 1997) and brown mosses (*Drepanocladus* sp.; Ellis et al. 2008). We studied 17 IWT ponds (with BYL24, BYL27, and BYL117 in more details) and 13 CP ponds (with BYL30 and BYL80 in more details). Shallow (0.1–0.3 m maximum depth) ponds forming in depressions of low-centered polygons during the snowmelt period (known as polygonal ponds) are also common in the study area. They are often short-lived or too shallow for common sampling approaches; nevertheless, a few were sampled for the diffusive

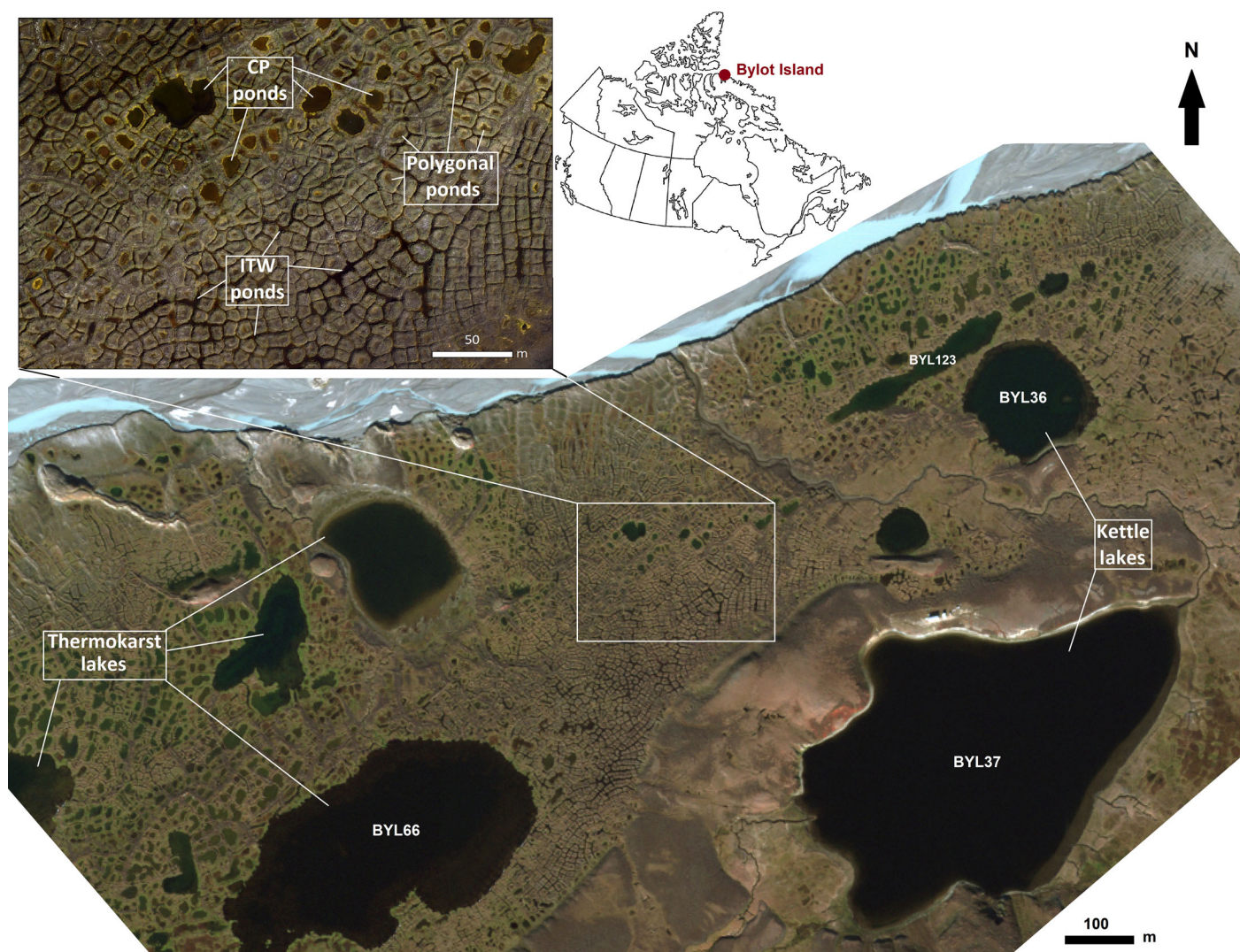


**Fig. 1.** Location map for Bylot Island and the study site, showing the abundance and diversity of water bodies in this landscape, including ice-wedge trough (IWT) and coalescent polygonal (CP) ponds. The zoomed area illustrates the complexity of pond structures found in tundra wetlands.

fluxes and were included in the same group as CP ponds, due to their similarities in morphology and biogeochemistry.

### Limnological data

The thermal structure of a few ponds and lakes (BYL27, BYL37, BYL66, and BYL80) was monitored for a minimum of 2 years (5-s to 1-h intervals) using submersible temperature loggers (RBR SoloT, Vemco Minilog-II-T, or Hobo U12, depending on the year and water body; specifications for all sensors are given in Table S1). In addition to these loggers recording annual cycles, manual measurements of temperature and dissolved oxygen (DO; ProODO, YSI Inc.) were carried out on all studied lakes and ponds with varying frequency during the field seasons. Limnological seasons were defined based on changes in the thermal structure of the water column (Table 3), also using seasonal patterns in DO, CO<sub>2</sub>, and CH<sub>4</sub> to validate and adjust the limits of these periods. The

length and timing of ice-out, mixing, and stratified periods can differ by 1–10 days between individual water bodies and years; hence for simplicity, these seasons are differentiated only between lakes and ponds. Briefly, spring corresponds to the period when ice is melting and the water column is mixing, early summer to the period when water is warming and the water column is stratifying (except for CP ponds, which are always mixed), and late summer to the period when the surface water is cooling but stratification is still present. Autumn corresponds to the turnover period before the ice-cover starts to form, which defines the start of the winter season. We acknowledge that these Arctic limnological seasons are different from climatological seasons, as well as seasons defined for temperate lakes.

Samples for other limnological characteristics, including concentrations of dissolved organic carbon (DOC), chromophoric fraction of dissolved organic matter (CDOM,

**Table 2.** Morphological and limnological characteristics of the studied water bodies, including surface area, maximum depth, mean depth, dissolved organic carbon concentration (DOC), absorbance coefficient at 320 nm ( $a_{320}$ ), absorption of DOM at 254 nm per unit DOC (SUVA), total suspended solids (TSS), total nitrogen (TN), total phosphorus (TP), and chlorophyll *a* concentration (Chl *a*). Median values of surface waters are presented for the four studied lakes and the most studied ponds, with additional group medians for all ice wedge trough ponds and coalescent polygonal ponds studied in the valley. Water bodies in bold corresponds to the one presented in Fig. 3. CP ponds, coalescent polygonal ponds; IWT ponds, ice-wedge trough ponds.

Water body type	Water body	Area	Max depth	Mean depth	DOC	$a_{320}$	SUVA	pH	TSS	TN	TP	Chl <i>a</i>
		m <sup>2</sup>	m	m	mg L <sup>-1</sup>	m <sup>-1</sup>	L m <sup>-1</sup> mgC <sup>-1</sup>		mg L <sup>-1</sup>	μg L <sup>-1</sup>	μg L <sup>-1</sup>	μg L <sup>-1</sup>
<b>Kettle lake</b>	<b>BYL36</b>	31,123	12.0	3.1	4.3	5.3	1.8	7.8	1.1	223.1	8.5	1.5
	BYL37	209,120	11.9	3.8	5.3	18.4	3.3	8.1	1.1	253.1	17.4	1.6
<b>Thermokarst lake</b>	<b>BYL66</b>	116,172	4.1	1.9	4.5	16.9	3.6	7.2	1.6	261.3	14.7	1.6
	BYL123	11,509	2.5	1.0	8.1	8.6	1.7	n.d.	1.3	584.6	20.3	n.d.
<b>IWT pond</b>	<b>BYL27</b>	> 400*	1.4	0.6	11.8	42.7	3.6	7.0	4.5	821.7	36.0	1.7
	BYL24	256	1.2	0.5	10.5	34.5	3.6	7.8	4.9	660.8	28.5	1.9
	Avg	20–300	0.8	0.4	12.7	37.6	3.1	7.3	5.4	828.4	30.7	2.0
	17 ponds											
<b>CP pond</b>	<b>BYL80</b>	212	0.8	0.6	10.9	12.7	1.8	8.9	2.8	915.1	22.2	0.8
	BYL30	125	0.7	0.4	12.2	24.9	2.3	8.6	2.7	798.6	19.8	1.6
	Avg	50–500	0.7	0.5	10.1	15.5	1.9	8.6	2.9	698.8	21.6	1.9
	13 ponds											

\*The limits of this pond are unclear due to the seasonal water level changes and persistent connections to other ponds, which may open or close from year to year depending on shore erosion.

characterized by the absorption coefficient at 320 nm and the specific UV absorbance index at 254 nm or SUVA), pH, total suspended solids (TSS), nutrients (total phosphorus, total nitrogen) and chlorophyll *a* (Chl *a*, as a proxy to phytoplankton biomass) were usually collected once a year in mid-July. Standard protocols were applied as described in Bouchard et al. (2015).

### Dissolved gas concentrations and diffusive flux estimations

Water samples for dissolved gas concentrations were obtained from the surface of all water bodies, sampling directly with the gas exchange bottle (see below). Deeper waters were also sampled (1) in ponds at 10-cm depth intervals using a thin-layer laminar-flow sampler that had two plates set 63.5 mm apart and connected to a peristaltic pump (Matveev et al. 2016), and (2) in lakes at 0.5-m depth intervals using a van Dorn water sampler (horizontal configuration, integrating 15 cm depth).

A water volume of 2 L was collected and equilibrated with 20 mL (2008–2015) or 30 mL (2016–2017) of atmospheric headspace for 3 min, using a low-density polyethylene Nalgene bottle with tubulation at the bottom connected to a syringe (Hesslein et al. 1991). The equilibrated gaseous headspace was injected into 6 mL (in 2008–2015) or 12 mL (in 2016–2017) gas-tight glass Exetainer vials, previously flushed with helium (2008–2014) or nitrogen (2015–2017) and vacuumed. In the laboratory, the headspace was analyzed by gas chromatography (GC) in a Varian 3800 from 2008 to 2015 (COMBIPAL headspace injection system, CP PoraPLOT Q 0.53 mm ID × 25 m,

flame ionization detector), or in a Thermo 1310 in 2016 and 2017 (TRI-Plus Head-Space auto-sampler, HSQ 80/100 1.6 mm × 30.5 m in series with MS 5A 1.6 mm × 18.3 m, thermal conductivity and flame ionization detectors). Dissolved gas concentrations were calculated using Henry's Law, and departure from saturation was obtained subtracting the gas concentration in the water at equilibrium with the atmosphere ( $C_{eq}$ ) using global annual average values of atmospheric partial pressures for each year based on data provided by the Earth System Research Laboratory (Dlugokencky and Tans 2017).

The diffusive flux ( $F_D$ , in mmol m<sup>-2</sup> d<sup>-1</sup>) was estimated using surface dissolved gas concentrations ( $C_{sur}$ ) and empirically estimated gas transfer coefficient ( $k_{600}$ ). Estimations of  $k_{600}$ , standardized to a Schmidt number ( $Sc$ ) of 600 (Waninkhof 1992), were calculated with the wind-based model proposed by Vachon and Prairie (2013):  $k_{600} = 2.51 + 1.48 U_{10} + 0.39 U_{10} \log_{10} LA$ , where  $U_{10}$  is the wind speed at 10 m above the ground (from a local meteorological station; CEN 2020) and  $LA$  is the lake surface area (km<sup>2</sup>); and applying the equation  $F_D = k (C_{sur} - C_{eq})$ , where  $k$  is the gas transfer coefficient for a given gas calculated as  $k = k_{600} (Sc/600)^{-1/2}$  for wind velocities > 3.7 m s<sup>-1</sup>, otherwise as  $k = k_{600} (Sc/600)^{-2/3}$ .

The study site is not accessible during the autumnal mixing period; hence, the latest (mid-August) gas concentrations in the water column were used to estimate the summer storage flux, assuming that all CO<sub>2</sub> and CH<sub>4</sub> accumulated in deeper layers would have sufficient time to mix with surface waters and equilibrate with the atmosphere before the ice cover

**Table 3.** Definition of the limnological seasons used in this study. Due to significant depth and volume differences among the water bodies, the timing of seasonal shifts differs between lakes and ponds. CP, coalescent polygonal; IWT, ice-wedge trough. Typical thermal structures are shown in Fig. 2.

Seasons on Bylot Island	Duration ( $\pm 5$ d) and description	
	Lakes	Ponds
<b>Spring</b> <i>Melting and mixing period</i>	<b>Jun 15–Jul 10.</b> This period begins when the ice cover starts to crack and melt, and ends when the last floating blocks of ice disappear. Water column keeps mixing and stays close to 4°C. Due to their larger volume, kettle lakes take up to a week longer to fully mix compared to thermokarst lakes. As the central part of the lakes remains ice-covered for a longer time, it was not possible to measure GHG concentration and ebullition flux during this period.	<b>Jun 15–Jul 1.</b> The completely frozen ponds start to thaw from the surface towards the bottom. The water level remains high as ponds are fed by melting snow but their lower section is still frozen, leading to a complex interconnected network of ponds (Fig. 8a). The shallow water column of IWT ponds quickly stratifies, despite the deeper parts being still frozen.
<b>Early summer</b> <i>Warming and stratification period</i>	<b>Jul 10–Aug 5.</b> Period of continuous warming of the water column. While thermokarst lakes maintain a well-mixed water column, deeper kettle lakes begin to form a thermal stratification in their deep basins (up to 5–7°C difference in late July).	<b>Jul 1–Aug 1.</b> Period during which the water column and sediments present a steady warming trend. The maximum surface water temperature is reached during the last week of July (17°C for IWT ponds; 23°C for CP ponds). CP ponds remain well-mixed. The water column of IWT ponds is strongly stratified (thermal gradient reaching 12°C m <sup>-1</sup> ); the stratification can be only partially broken on cool, cloudy days when wind is aligned with the pond axis (but bottom waters never rise above 4°C).
<b>Late summer</b> <i>Cooling period</i>	<b>Aug 5–Aug 25.</b> This period begins with the warmest water column of the year, after which it slowly starts cooling down. The thermokarst lakes continue mixing, but weak stratification is possible during calm and warm weather (discontinuous cold polymictic lakes). Kettle lakes continue having stratified deeper basins.	<b>Aug 1–Aug 15.</b> With the sun starting to sink below the horizon, the difference in surface water temperatures between mornings and evenings increases, with an occasional thin ice cover observed in the morning. This period is marked with a general drop in water column temperatures, and in less stable stratification in IWT ponds.
<b>Autumn</b> <i>Mixing period before freezing</i>	<b>Aug 25–Oct 1.</b> Water temperature drops significantly at the beginning of this period and stays low (0–5°C). Water column keeps mixing. The period ends when the ice cover becomes permanent.	<b>Aug 15–Sept 15.</b> Period marked by a significant drop in water temperature, followed by intermittent mixing in IWT ponds lasting up to 2 weeks. The period ends when the ice cover becomes permanent.
<b>Winter</b> <i>Ice-covered period</i>	<b>Oct 1–Jun 15.</b> A layer of water remains under ice. Water temperatures keep dropping during this period (down to 2°C in kettle lakes and close to 0°C in the thermokarst lake).	<b>Sept 15–Jun 15.</b> Freezing progresses from all directions (inward freezing). Hydraulic pressure fractures the ice and forces water to spring out to the surface, creating ice mounds (Fig. 6d). Ponds remain completely frozen from October until next spring.

forms. The theoretical autumnal surface concentration was calculated by mixing epilimnetic with hypolimnetic gas concentrations, with the volume of each water layer calculated from hypsographic curves. Similarly, the CO<sub>2</sub> and CH<sub>4</sub> measurements in the ice cover and under the ice (obtained during late-winter campaign from 22 May to 2 June 2015) were used to

calculate the winter storage flux for the two lakes (BYL66 and BYL36), again assuming a full transfer of the accumulated gas to the atmosphere and taking into account the volumetric proportions of the ice and underlying water mass. Storage fluxes were estimated using the equations above, with wind velocities averaged over the mixing period of each lake or pond.

The majority of dissolved CO<sub>2</sub> and CH<sub>4</sub> data comes from day-time sampling; out of the 453 measurements included in the study (all water bodies and dates combined), 78 values were from night-time sampling (9 p.m. to 6 a.m., period defined when solar irradiance was below ~33% of zenith), allowing a fair assessment of diurnal variations. A formal diurnal cycle following surface concentrations of CO<sub>2</sub> and O<sub>2</sub> over a 6-d period was additionally obtained from IWT pond BYL24 in July 2008 using a continuous gas monitoring system, further described in Bastien et al. (2008) and Laurion et al. (2010). Briefly, the system was equipped with a CO<sub>2</sub> infrared gas analyzer (LI820, LI-COR) and an O<sub>2</sub> sensor (Qubit Systems), both installed on a gas stream equilibrated with the source water. Surface water was pumped at 20 cm depth via a reversible peristaltic pump controlled with solenoid valves, filtered using layers of Nitex of 250, 100, 53, and 10 μm, and passed through a bundle of porous polypropylene tubes that act as a

water-air exchanger. Water and air temperatures were also recorded. Measurements were taken automatically every 3 h.

### Ebullition flux measurements

Ebullition gas samples were collected using submerged funnels (as in Bouchard et al. 2015; based on Wik et al. 2013) equipped with a 140-mL polypropylene plastic syringe and deployed for a period of 6 h to 2 weeks depending on the flux rate (5 d as median duration; 15% of cases exceeding 10 d). The possibility of a slow dissolution of the CH<sub>4</sub>-enriched gas accumulated in the syringe back into water on long deployments was tested by looking at the relationship between ebullition collection time and the CO<sub>2</sub> to CH<sub>4</sub> ratio, which was not significant (*p* value = 0.640). Most importantly, long deployments in kettle lakes still showed on average seven times higher CO<sub>2</sub> concentration in the syringe compared to

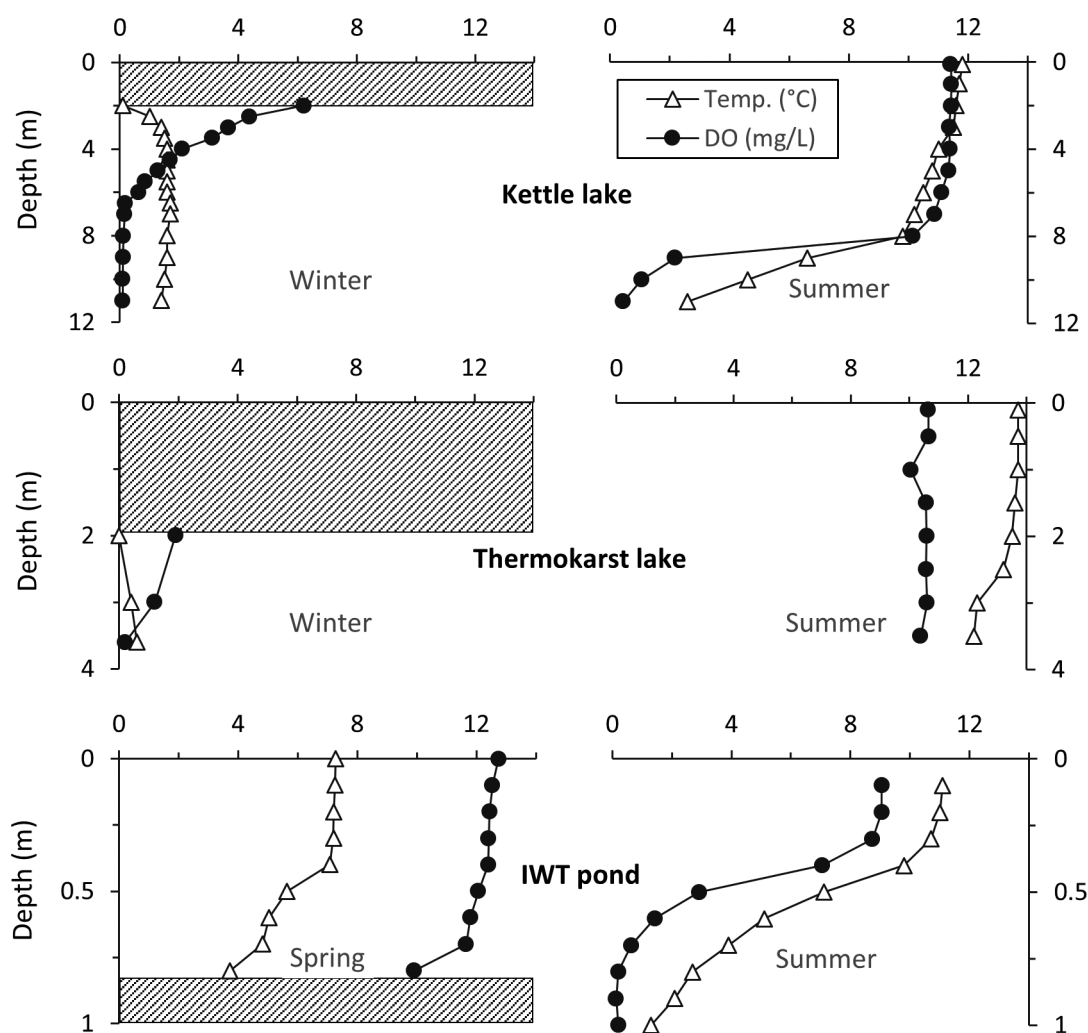


**Fig. 2.** Examples of typical temperature and dissolved oxygen (DO) profiles for the three water body types presenting a vertical structure. Late winter and late summer are presented for the kettle lake BYL36 (6 June 2015 and 28 July 2016) and the thermokarst lake BYL66 (2 June 2015 and 3 August 2016), while spring and late summer are presented for the IWT pond BYL27 (27 June 2015 and 3 August 2016).

surface waters, despite the high solubility of CO<sub>2</sub> in water. The small headspace–water contact area in the syringe likely slowed down dissolution rate.

The same vials described above were used to collect gas samples for GC analysis. Ebullition flux ( $F_E$ , in  $\text{mmol m}^{-2} \text{d}^{-1}$ ) was calculated as  $F_E = p\text{GHG} \times V/A \times V_m \times t$ , where  $p\text{GHG}$  is the partial pressure of CO<sub>2</sub> or CH<sub>4</sub> measured with the GC,  $V$  is the total collected gas volume over the accumulation time  $t$ ,  $A$  is the funnel area, and  $V_m$  is the molar gas volume at ambient air temperature. Ebullition was monitored during the ice-free period in all 4 studied lakes and in 14 ponds (9 IWT

and 5 CP ponds) that were deep enough for the installation of funnels. Ebullition could not be assessed in lakes during the melting period (due to moving ice floes); therefore, their spring flux consists only of the diffusive flux. In comparison to the diffusive fluxes that are biased toward daytime hours, ebullition fluxes typically integrate many days and thus comprise both day-time and night-time emissions.

### Radiocarbon and stable isotopes analyses

At the beginning and end of each field season, a fraction of the ebullition samples collected from the funnels were

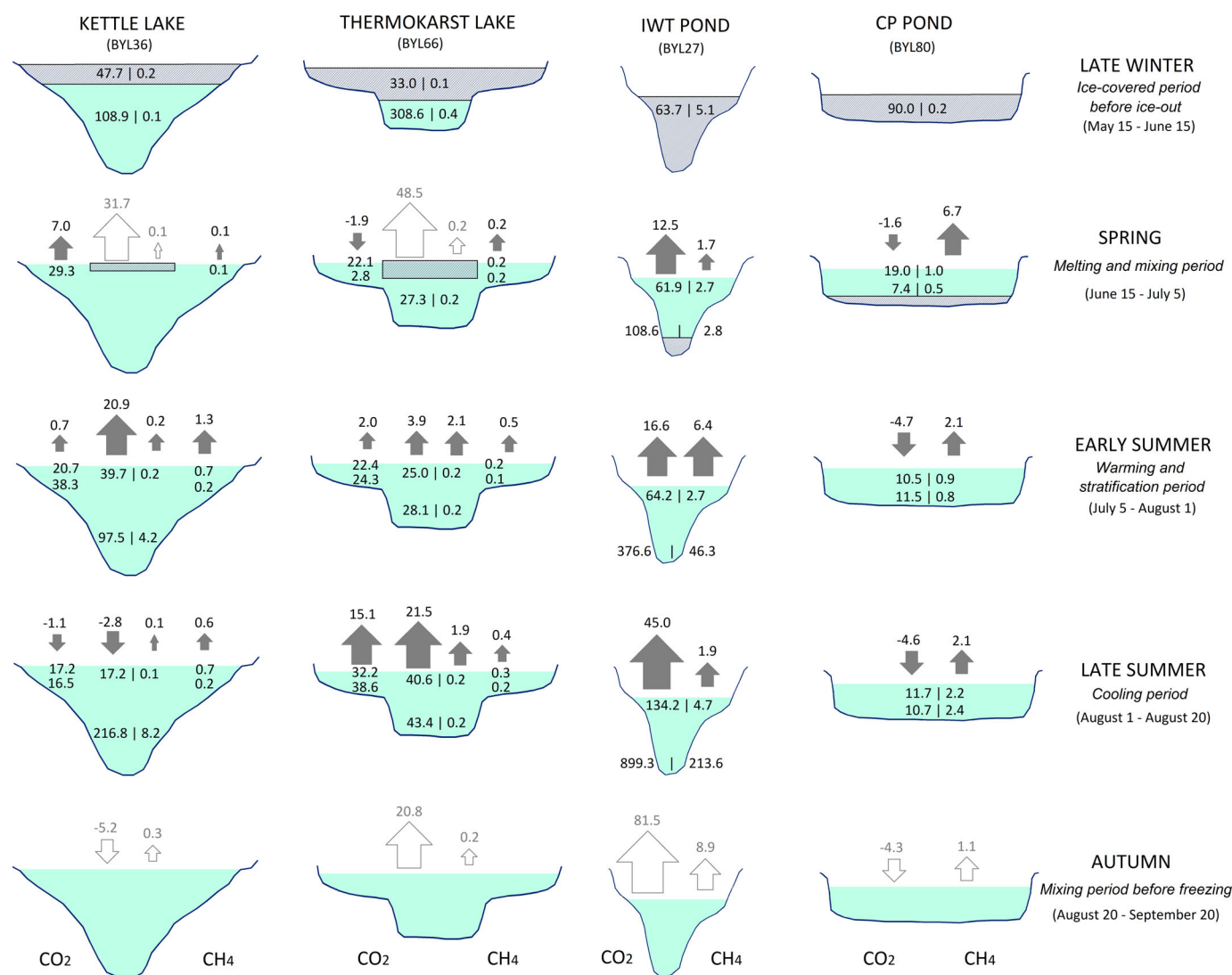


**Fig. 3.** Seasonal variations in CO<sub>2</sub> and CH<sub>4</sub> concentrations (values presented in the water column, in  $\mu\text{M}$ ) and fluxes (values above the arrows, in  $\text{mmol m}^{-2} \text{d}^{-1}$ ) from the four studied water body types. The CO<sub>2</sub> fluxes (or concentrations) are given by the arrows (or numbers) on the left of each water body, and CH<sub>4</sub> fluxes (or concentrations) by the arrows (or numbers) on the right. The dissolved gas concentration values, when available, are presented for the surface (upper 10 cm) and bottom (lower 10% of the total depth) waters, and in the case of lakes, are further distinguished between shallow and deep zones. Filled arrows indicate the recorded fluxes (sum of diffusion and ebullition, based on in situ measurements), whereas empty arrows denote the estimated storage fluxes (i.e., not directly measured). The size of the arrows is proportional to the strength of the fluxes, but not using a linear scale, with the CH<sub>4</sub> scale amplified by two relative to CO<sub>2</sub>. Water body shapes are not to scale between the different types. The water body filling represents water (light blue) or ice (grey). The limnological seasons used here are further explained in detail in Table 3.

transferred into 50-mL glass bottles closed with thick butyl rubber stoppers (bottles were acid-washed, precombusted, helium-flushed and vacuumed) and sent to the Keck Carbon Cycle AMS facility at the University of California, Irvine for radiocarbon ( $^{14}\text{C}$ ) and  $^{13}\text{C}$  isotopic ratio analyses for  $\text{CO}_2$  and  $\text{CH}_4$  (detailed protocol description in Pack et al. 2015).

Dissolved gas samples were also collected for  $^{14}\text{C}$  and  $^{13}\text{C}$  analyses. Dissolved  $\text{CO}_2$  samples were collected “passively” using zeolite molecular sieve traps installed in selected water bodies (3 lakes and 9 ponds) over a period of 51 d (25 June–15 August 2015). The method, which slowly traps dissolved  $\text{CO}_2$  in the water column over an extended time period is described in detail in Garnett et al. (2012). The zeolite pellets are contained within a glass tube sealed at both ends by gas-permeable, water-

impermeable hydrophobic filters. The molecular sieves, enclosed within a robust, protective, open polyvinyl chloride tube, were installed at 25 cm depth in the selected water bodies. After placing below the water surface, a clip is removed to allow ingress of  $\text{CO}_2$ ; when the sampling period was over, the clip was replaced underwater to avoid contamination by atmospheric  $\text{CO}_2$ . The molecular sieves and their protective housing were returned to the NERC Radiocarbon Laboratory in Scotland, where the  $\text{CO}_2$  was recovered by heating and cryogenic purification, prior to the determination of  $^{13}\text{C}$  and  $^{14}\text{C}$ . Discrete samples of  $\text{CH}_4$  were also collected using the “super headspace” method (Garnett et al. 2016a) involving equilibrating several large volumes of water samples with ambient air in 15-L collapsible water containers from three ponds where  $\text{CH}_4$  concentration was

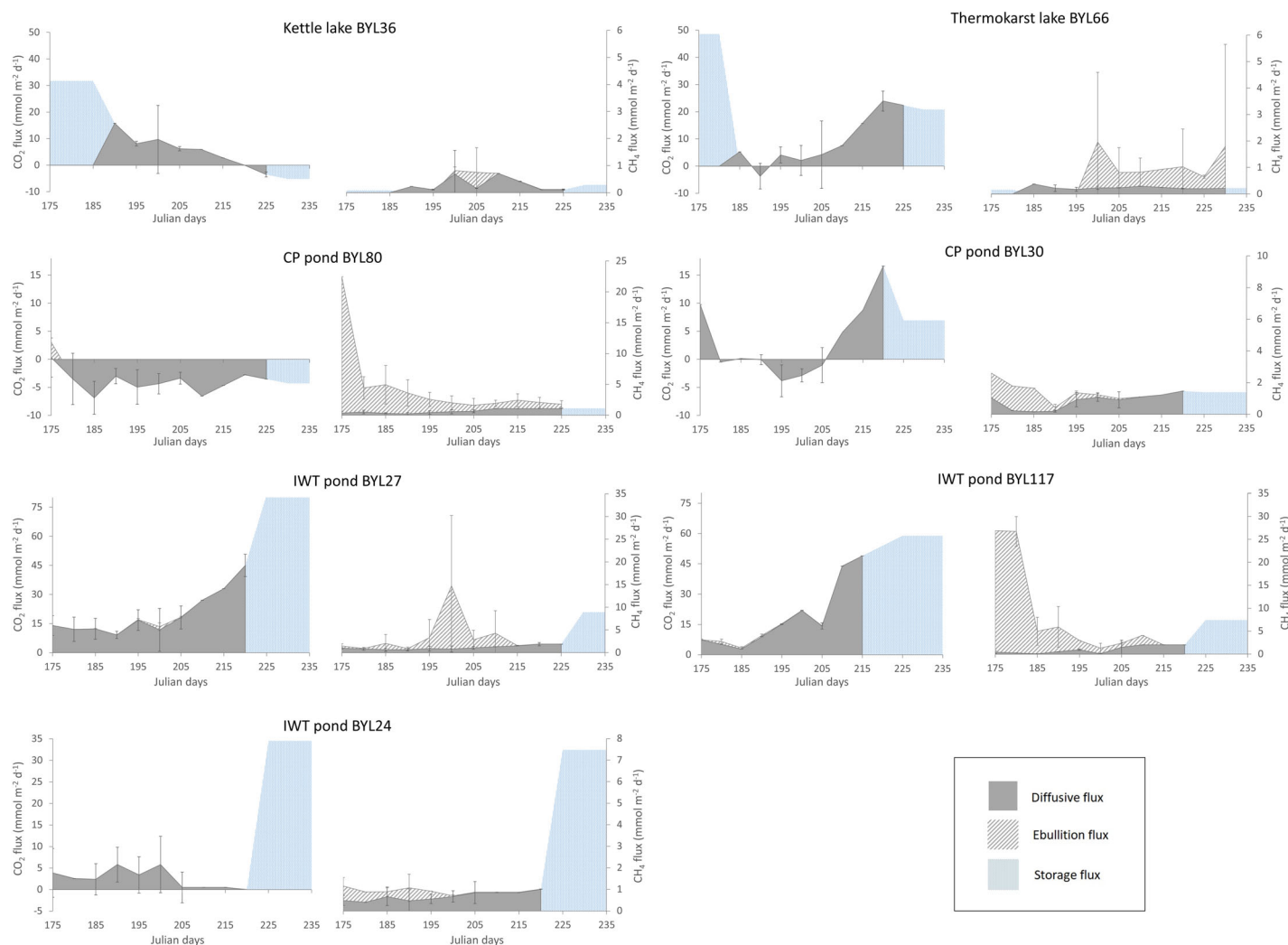


**Fig. 4.** Temporal variations in  $\text{CO}_2$  and  $\text{CH}_4$  fluxes from seven water bodies, in which sufficient data were available to present trends in diffusive flux (dark grey area) and ebullitive flux (dashed area on top of diffusive flux). Estimated late-season fluxes are also added (pale grey area). The fluxes are 5-d period averages merging different years together; hence, the error bars representing the standard deviations illustrate both the intra and inter-annual variations. Littoral and pelagic values for lakes BYL66 and BYL36 were averaged, taking into account their proportions to the total lake surface area. Ebullition fluxes are missing prior to the 195<sup>th</sup> Julian day for the two lakes, because the ice floes hindered the installation of bubble traps. Note that flux scales differ among water bodies.

**Table 4.** Average greenhouse gas diffusive and ebullition fluxes for the studied water bodies (specific values and standard deviations are given in Table S2). These averages are based on discrete flux measurements (i.e., storage fluxes not included). The total GHG flux normalized by the global-warming potential of each gas (named the GWP index, given in CO<sub>2</sub> equivalent, CO<sub>2</sub> eq.) includes both diffusive and ebullition fluxes, where CH<sub>4</sub> was assumed to be 32 times more potent than CO<sub>2</sub> (on a gram-to-gram basis over 100 years; Nisbet et al. 2019). Water bodies in bold correspond to the ones presented in Fig. 3. CP ponds, coalescent polygonal ponds; IWT ponds, ice-wedge trough ponds; *N*, number of measurements.

Water body		Diffusive flux (mmol m <sup>-2</sup> d <sup>-1</sup> )			Ebullition flux (mmol m <sup>-2</sup> d <sup>-1</sup> )			GWP <sub>100</sub> index (mmol CO <sub>2</sub> eq. m <sup>-2</sup> d <sup>-1</sup> )*
Type	Name	<i>n</i>	CO <sub>2</sub>	CH <sub>4</sub>	<i>n</i>	CO <sub>2</sub>	CH <sub>4</sub>	
Kettle lakes	<b>BYL36</b>	16	4.988	0.360	18	0.004	0.131	10.8
	BYL37	11	23.39	0.108	6	0.005	0.040	15.2
Thermokarst lakes	<b>BYL66</b>	22	3.455	0.213	29	0.013	1.462	27.1
	BYL123	2	-9.251	0.430	10	0.011	0.186	-0.2
IWT ponds	<b>BYL27</b>	75	16.09	0.955	31	0.408	3.837	60.5
	BYL117	13	15.16	0.930	21	0.420	5.255	93.9
	BYL24	45	3.599	0.613	19	0.010	0.326	14.3
	Average 17 ponds	224	12.74	0.890	84	0.261	2.844	n/a
CP ponds	<b>BYL80</b>	68	-4.110	0.479	39	0.106	2.550	49.1
	BYL30	18	-0.119	0.775	10	0.017	0.489	16.7
	Average 13 ponds	161	-4.051	0.555	61	0.070	1.844	n/a

\*To calculate the GWP<sub>100</sub> index, individual flux values were first converted to CO<sub>2</sub> equivalent before computing the average. These values do not include the estimated spring and autumn fluxes from cumulated gases under the ice or in the hypolimnion, but only directly measured fluxes.

**Table 5.** Radiocarbon contents of dissolved organic carbon (DOC), and dissolved and ebullition CO<sub>2</sub> and CH<sub>4</sub>. <sup>14</sup>C ages are given in YBP (numbers above) and fraction modern (numbers below); each given range is composed of two dates only. Measurement errors can be found in data repository Prėskienis et al. (2020). Gas samples from littoral (L) and pelagic (P) zones were analyzed for the thermokarst lake BYL66, but in the kettle lake BYL36 only the littoral zone provided enough ebullition carbon for <sup>14</sup>C analysis. CP ponds, coalescent polygonal ponds; IWT ponds, ice-wedge trough ponds; n.d., not determined.

Water body		<sup>14</sup> C age (YBP above, and fraction modern under)							
Type	Name	Zone	DOC	Diss. CO <sub>2</sub>	Ebul. CO <sub>2</sub>		Diss. CH <sub>4</sub>	Ebul. CH <sub>4</sub>	
					Early July	Late July		Early July	Late July
Kettle lake	BYL36	L	756	441	n.d.	970	n.d.	n.d.	125–2015
			0.910	0.947		0.886		0.778–0.984	
Thermokarst lake	BYL66	L	108	282	390–540	1790	n.d.	1555–2775	1500
			0.987	0.966	0.935–0.952	0.801		0.708–0.824	0.734
		P			735–765	510–1960	n.d.	3105–3380	2480–3405
					0.909–0.913	0.939–0.784		0.657–0.679	0.655–0.829
IWT ponds	BYL27		34	Modern	35–165	Modern–170	Modern	Modern–5	Modern
			0.996	1.013	0.996–0.979	0.979–1.009	1.009	0.999–1.037	1.006–1.015
	BYL117		47	24	240	240	Modern	Modern	Modern
			0.994	0.997	0.97	0.97	1.007	1.003	1.006
	BYL24		Modern	Modern	Modern	Modern–1340	Modern	Modern	Modern
			1.037	1.065	1.005	0.846–1.049	1.035	1.035	1.041–1.043
CP ponds	BYL80		Modern	Modern	Modern	245–1220	n.d.	Modern	Modern
			1.015*	1.034*	1.046	0.859–0.97		1.063–1.067	1.059–1.076
	BYL30		Modern	Modern	Modern	20	n.d.	Modern	Modern
Polygonal ponds (n = 3)			1.028	1.033	1.026	0.997		1.061–1.073	1.063
			Modern	Modern	n.d.	n.d.	n.d.	n.d.	n.d.
			1.066	1.049					

\*There are no dates available from BYL80 for DOC and dissolved GHG; however, dates were obtained on a few coalescent ponds with a similar morphology, therefore the average (n = 3) CP ponds values are presented here.

known to be sufficiently elevated. Headspace  $\text{CH}_4$  concentration was measured using a portable Detecto Pak-Infrared gas analyzer, and the  $\text{CH}_4$ -enriched headspace (4 L) stored in large 10-L air-tight gas sample bags. The gas sample bags were sent to the NERC radiocarbon laboratory for analysis. Further details of the recovery of  $\text{CO}_2$  and  $\text{CH}_4$  for isotope analysis are given in Garnett et al. (2016a,b).

An additional series of gas samples collected from melted ice, ebullition funnels, lake sediments or dissolved in water were analyzed for isotopic composition ( $^{13}\text{C}$  of  $\text{CO}_2$ , and  $^{13}\text{C}$  and  $^2\text{H}$  of  $\text{CH}_4$ ) using gas chromatography-isotope ratio mass spectrometry (Thermo GC-IsoLink coupled to a Delta V Plus) at the McGill University Isotope Biogeochemistry Laboratory, following methods described by Kinnaman et al. (2007) and Ai et al. (2013). A volume of 10–500  $\mu\text{L}$  of gas was injected into the GC using a pressure and temperature variable

injector. Gases were separated using a GS Carbon Plot column at 35°C following the method of Ai et al. (2013), and  $\text{CH}_4$  was either combusted to  $\text{CO}_2$  at 1000°C (for  $\delta^{13}\text{C}$ ) or pyrolysed to  $\text{H}_2$  at 1400°C (for  $\delta^2\text{H}$ ). Isotope values were converted to the VPDB and VSMOW scales using a two-point calibration based on isotopic standards (AirLiquide Inc.).

DOC was also collected for isotopic analyses of  $^{14}\text{C}$  and  $^{13}\text{C}$  at the Woods Hole NOSAMS facility (2013 dates), the NERC radiocarbon facility (2015 dates), or the Lalonde AMS laboratory (2017 dates). Isotopic analysis of DOC involved acidification of the sample to pH 4 to remove any inorganic carbon, rotary evaporation, and freeze drying, prior to combustion at 900°C to  $\text{CO}_2$  followed by graphitization.

A portion of the presented radiocarbon and stable isotope data (from 2013 and 2014 field campaigns), published in Bouchardeau et al. (2015), are used here in combination with data

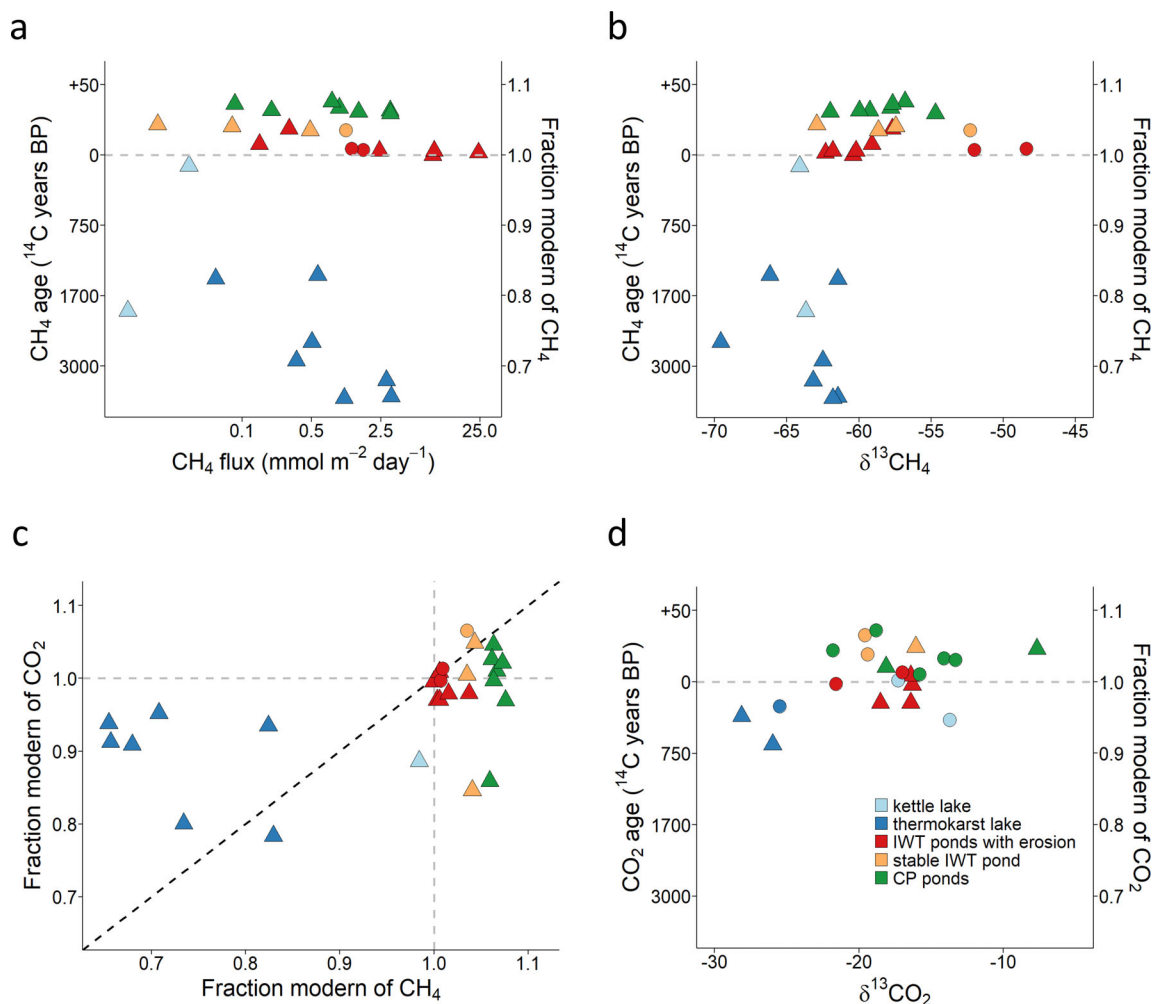


**Fig. 5.** Variations among water body types in  $\text{CH}_4$  signatures and fluxes (a); relationship between  $\text{CH}_4$  radiocarbon and stable isotopic signatures (b), between radiocarbon signatures of  $\text{CH}_4$  and  $\text{CO}_2$  with the dashed diagonal line representing a ratio of 1 (c), and between  $\text{CO}_2$  radiocarbon and stable isotopic signatures (d). The same colours are used in all four graphs to represent the different water body types, with triangles indicating ebullitive GHG and circles representing dissolved GHG. Note that due to the wide range in  $\text{CH}_4$  flux (a), the x-axis has been transformed to logarithmic scale. Horizontal and vertical grey dash lines represent fraction modern = 1 ( $^{14}\text{C}$  age = 0), with fraction modern > 1 indicating the presence of bomb  $^{14}\text{C}$ .

from samples collected in 2015 and 2016, allowing a better exploration of seasonal trends.

## Results

The thermal structure of the different water body types is illustrated in Fig. 2. Temporal and spatial trends in CO<sub>2</sub> and CH<sub>4</sub> are presented in Fig. 3 (seasonal trends of gas concentrations and fluxes in four water bodies, differentiating pelagic and littoral zones of the lakes) and in Fig. 4 (detailed temporal trends in diffusive and ebullition fluxes in seven water bodies), while averages are presented in Table 4 (and seasonal averages with standard deviations in Table S2). All individual data can

be retrieved in Nordicana D data repository Prėskienis et al. (2020).

### Kettle lakes

The CO<sub>2</sub> fluxes from the kettle lakes were highest during spring, remained high early summer, and then decreased progressively, with negative CO<sub>2</sub> fluxes (small sinks of CO<sub>2</sub>) becoming increasingly frequent by the end of July (Fig. 4). Emission of CH<sub>4</sub> remained generally low (0.1–0.8 mmol m<sup>-2</sup> d<sup>-1</sup>) and principally occurred through diffusion (on average 80% of total CH<sub>4</sub> emissions); the only exception being early summer along the shores of the smaller kettle lake, BYL36,

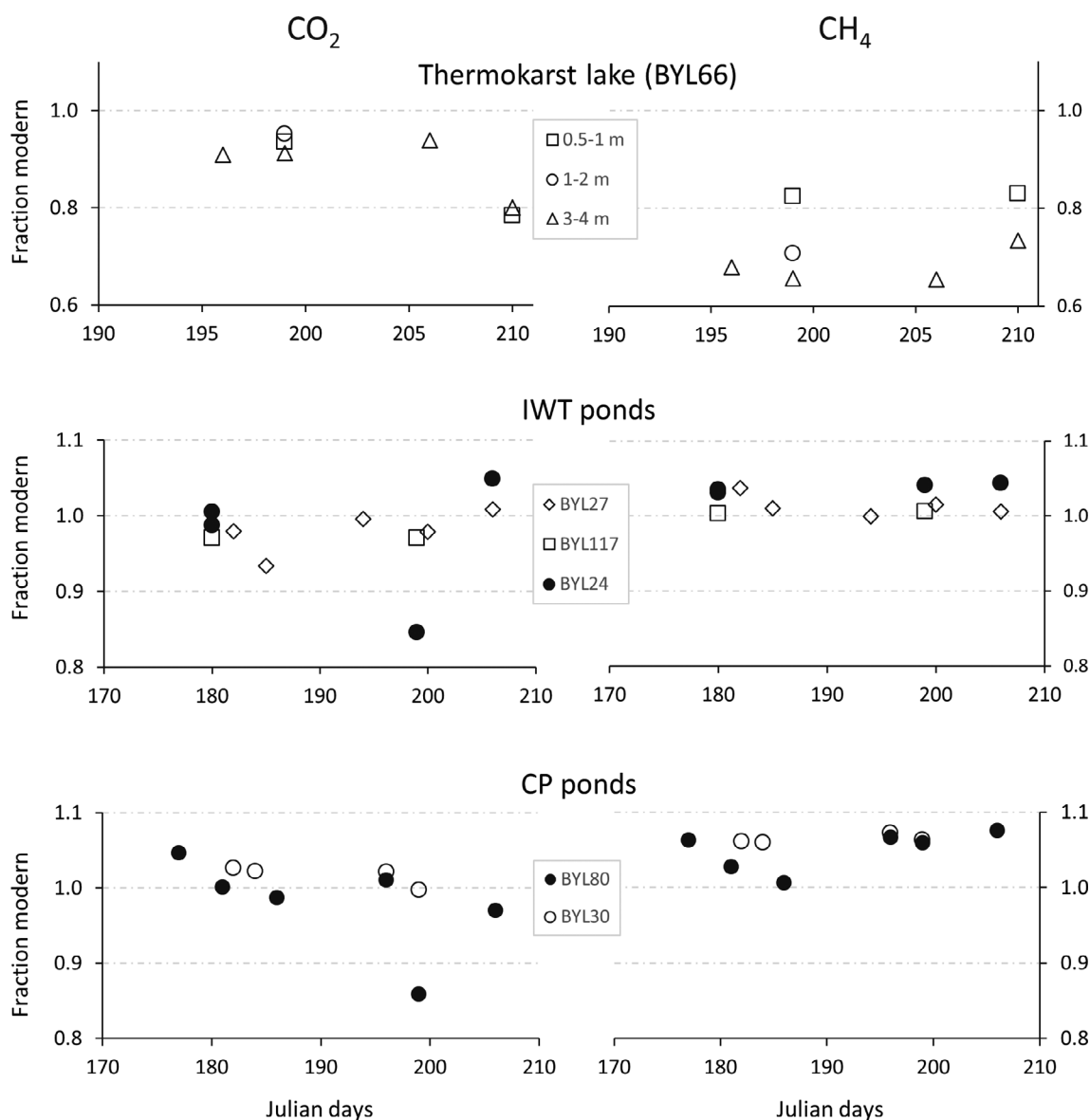


**Fig. 6.** Radiocarbon signature (fraction modern) of ebullition GHG along the open-water season. The temporal patterns of fraction modern of CO<sub>2</sub> are given on left panels, and of CH<sub>4</sub> on right panels. Each point denotes a single measurement. Analytical errors vary from 0.0011 to 0.0109, not visible in the plots.

**Table 6.** Stable isotopic compositions of dissolved organic carbon (DOC), and dissolved and ebullition greenhouse gases. Water bodies in bold correspond to the ones presented in Fig. 3. Averages of all available data are presented for both ponds types. CP ponds = coalescent polygonal ponds; IWT ponds, ice-wedge trough ponds; *n*, number of values composing the average.

Water body		DOC		Dissolved GHG			Ebullition GHG	
Type	Name	$\delta^{13}\text{C}$	$\delta^{13}\text{C}$		$\delta^2\text{H}$	$\delta^{13}\text{C}$		$\delta^2\text{H}$
			$\text{CO}_2$	$\text{CH}_4$	$\text{CH}_4$	$\text{CO}_2$	$\text{CH}_4$	$\text{CH}_4$
Kettle lakes	<b>BYL36</b>	-27.6	-14.6	-51.9	-357.0	-16.3	-62.3	-350.0
	BYL37	-28.3	-17.3	n.d.	n.d.	-18.5	n.d.	n.d.
Thermokarst lake	<b>BYL66</b>	-28.0	-21.3	-53.8	-324.2	-24.0	-63.4	-328.4
IWT ponds	<b>BYL27</b>	-27.5	-15.8	-50.5	-345.5	-16.1	-59.7	-407.1
	BYL117	-28.1	-17.6	-52.0	-344.6	-17.5	-62.3	-389.8
	BYL24	-28.1	-18.2	-52.3	-319.5	n.d.	-60.3	-374.8
	Average	-27.9 ( <i>n</i> = 4)	-17.0 ( <i>n</i> = 20)	-49.3 ( <i>n</i> = 19)	-349.2 ( <i>n</i> = 11)	-17.0 ( <i>n</i> = 3)	-60.7 ( <i>n</i> = 13)	-394.7 ( <i>n</i> = 8)
	IWT ponds							
CP ponds	<b>BYL80</b>	-25.9	n.d.	n.d.	n.d.	-3.8	-58.9	-359.7
	BYL30	-26.5	-14.1	-46.2	-310.9	-17.2	-60.0	-355.6
	Average	-26.4 ( <i>n</i> = 6)	-15.0 ( <i>n</i> = 15)	-46.3 ( <i>n</i> = 9)	-333.0 ( <i>n</i> = 8)	-10.5 ( <i>n</i> = 4)	-59.9 ( <i>n</i> = 18)	-353.9 ( <i>n</i> = 11)
	CP ponds							

where ebullition represented 60% of total  $\text{CH}_4$  emissions (Fig. 3). Although the stratified water column (Fig. 2) allowed GHG accumulation at the bottom, it did not result in increased autumnal emissions due to the small volume of the hypolimnion (2% of the total lake volume).

The kettle lake BYL36 presented the oldest radiocarbon age for DOC (756 YBP) and dissolved  $\text{CO}_2$  (441 YBP) among all aquatic systems sampled in the valley (Table 5). Ebullition rates were often too low to collect sufficient carbon for radiocarbon analysis; however the few dates obtained along the littoral zone were in the same range (125–2015 YBP) for ebullition gases.

### Thermokarst lakes

The  $\text{CO}_2$  fluxes from the larger thermokarst lake BYL66 were also highest during spring, but in contrast to the kettle

lakes, they decreased right after the ice-out and later showed a rising trend (Fig. 4). Early in the season, the shallow zone of Lake BYL66 tended to be a sink of  $\text{CO}_2$  more often than a source (from  $-7$  to  $+5 \text{ mmol m}^{-2} \text{ d}^{-1}$ ); however, positive fluxes to the atmosphere became more common as summer progressed. For comparison, the more transparent thermokarst Lake BYL123 (higher DOC but much lower SUVA; Table 2) continued to uptake  $\text{CO}_2$  even later in summer. Since these lakes are well-mixed throughout the warm season (BYL66 qualified as a discontinuous cold polymictic lake), bottom and surface  $\text{CO}_2$  concentrations followed the same trend and slowly increased during summer (Fig. 3). Dissolved  $\text{CH}_4$  concentrations remained relatively low and did not show any clear trends over time. However, the dominant  $\text{CH}_4$  emission pathway from Lake BYL66 was via ebullition (26–54% for the

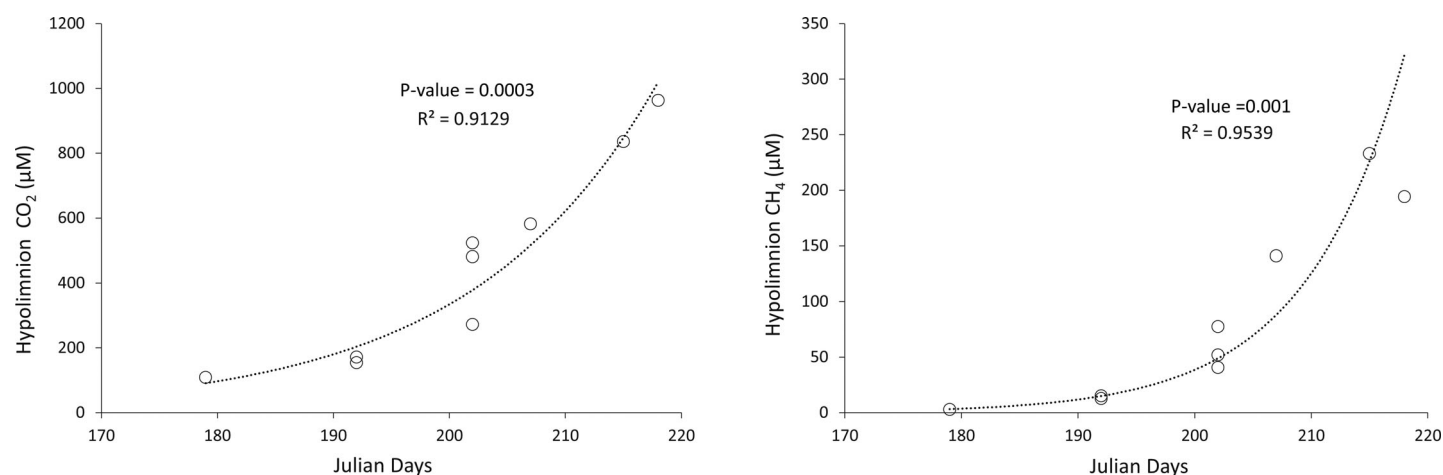


**Fig. 7.** The seasonal increase in concentrations of  $\text{CO}_2$  (left) and  $\text{CH}_4$  (right) in hypolimnetic waters of the most studied IWT pond BYL27.

littoral zone, and 88–91% for the deep zone). The deep central basin had similar ebullition rates as ponds (on average  $1.9 \text{ mmol of CH}_4 \text{ m}^{-2} \text{ d}^{-1}$ ), while in the littoral zone of the lake ( $< 2 \text{ m}$ ) rates were lower ( $< 0.58 \text{ mmol of CH}_4 \text{ m}^{-2} \text{ d}^{-1}$ ; Fig. 3) and comparable to fluxes measured from Lake BYL123 (Table 4).

The ebullition flux from Lake BYL66 was not only relatively high, but also characterized by a more depleted  $^{14}\text{C}$  signature of  $\text{CH}_4$  compared to the other studied water bodies (Fig. 5a). In general, ebullition gases were much older than DOC or dissolved  $\text{CO}_2$  (108 and 282 YBP, respectively). Ebullitive  $\text{CO}_2$  radiocarbon age ranged from 400 to 2000 YBP (Table 5), with

no clear spatial variation (deep and shallow basins emit  $\text{CO}_2$  of similar ages), but with a slightly older signature later in the summer (Fig. 6). The  $^{14}\text{CH}_4$ , on the other hand, did not present any temporal trend, but deeper sections of the lake emitted older  $\text{CH}_4$  (2500–3500 YBP) compared to the shallow zones (1400–2800 YBP). Moreover, BYL66 had lower  $\delta^{13}\text{CO}_2$  values compared to the other water body types ( $-28\text{‰}$  to  $-17\text{‰}$ ; Fig. 5d). The range of  $\delta^{13}\text{CH}_4$  values was close to that of kettle lakes ( $-67\text{‰}$  to  $-54\text{‰}$ ) with one ebullition value dropping to  $-71\text{‰}$  (Fig. 5b). The  $\delta^2\text{H}$  of  $\text{CH}_4$  included some of the highest values recorded for this study site ( $-387\text{‰}$  to  $-269\text{‰}$ , Table 6).

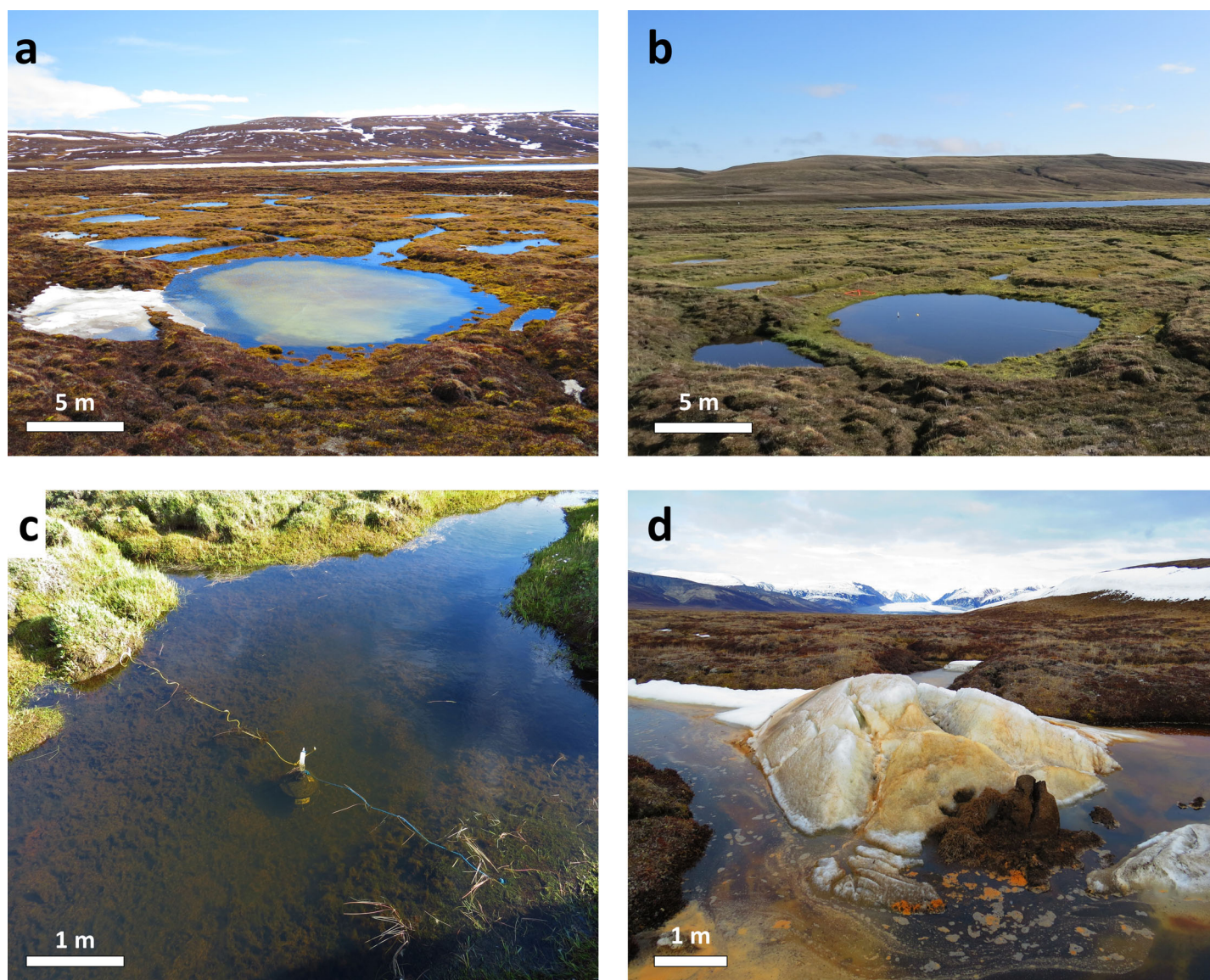


**Fig. 8.** Photos illustrating the landscape differences between snow-melting season (a) and peak summer (b) near CP pond BYL30; an example of a stable IWT pond colonized by brown mosses (c); and a frost mound melting in an IWT pond (d; photo taken during spring melt). IWT ponds can interconnect with each other, as well as with CP ponds (a). With summer progressing, ponds become isolated (b). The dark orange photosynthesizing microbial mat forming on the ice surface can be seen (a).

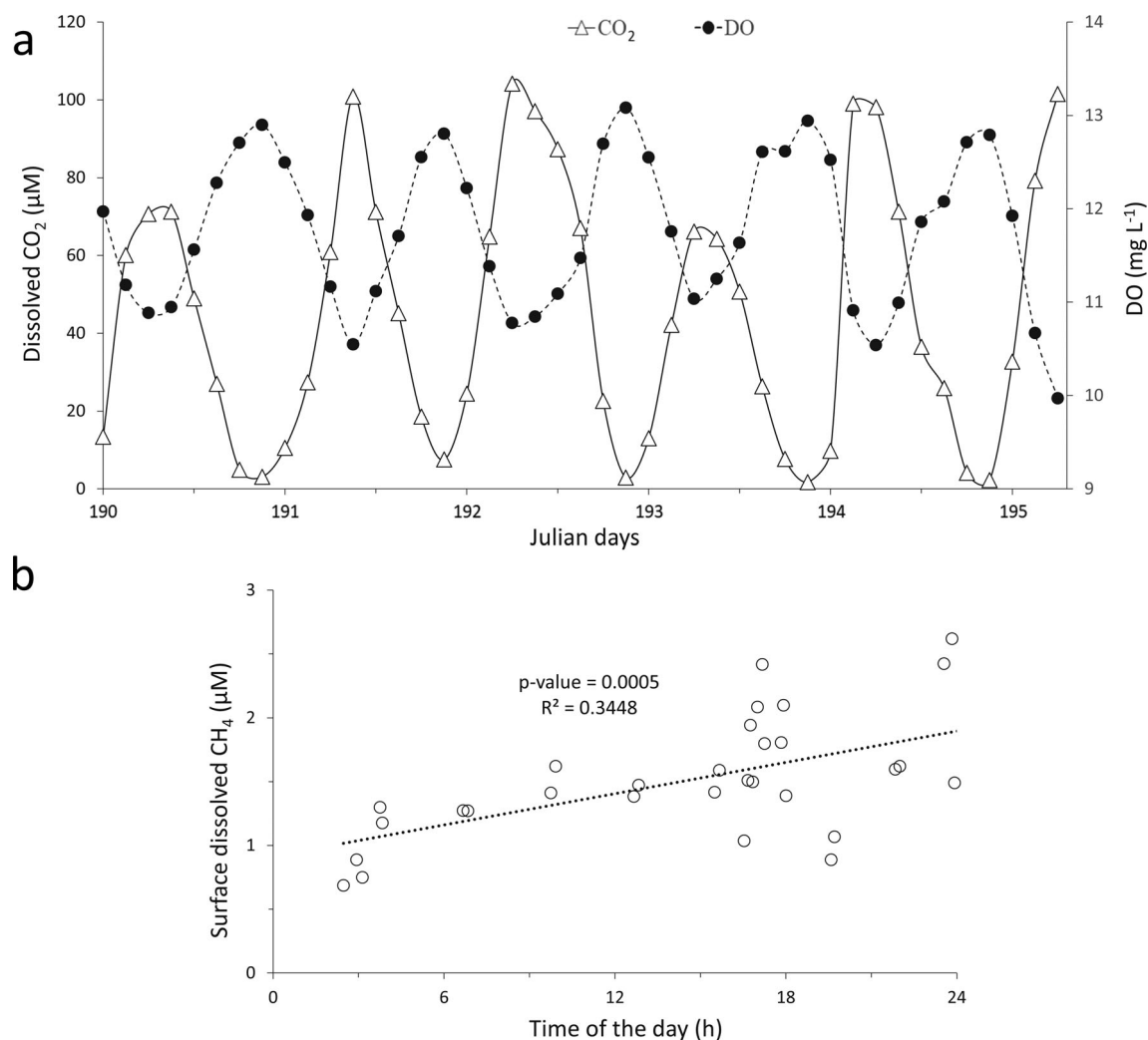


**Fig. 9.** Diurnal variations in concentrations of CO<sub>2</sub> and dissolved oxygen (DO) in surface waters of the IWT pond BYL24, during mid-July (a). Increasing CH<sub>4</sub> concentration in the CP pond BYL80 during daytime (b); the data set is composed of discrete values taken over many days (of July) and several years.

### Ice-wedge trough ponds

Elevated dissolved CO<sub>2</sub> and CH<sub>4</sub> concentrations and high ebullition rates were recorded immediately after the ponds started to thaw in spring (thawing occurs from top to bottom in ponds, with the ice layer on the pond bottom in spring, as illustrated in Figs. 2, 3). Diffusive fluxes increased over time toward the autumn, while ebullition rates slowed down progressively during the summer (Fig. 4). Therefore, the contribution of ebullition to the total CH<sub>4</sub> flux decreased over time (from 60–90% in early summer to 1–50% in late summer). Due to the continuous thermal stratification observed in IWT ponds (typical thermal structure illustrated in Fig. 2), bottom water GHG concentrations rose exponentially during July (Fig. 7). This led to extremely high summer storage fluxes estimated for the autumnal mixing period (Figs. 3, 4), which lasted from 4 to 14 d depending on individual ponds and specific years (obtained from the continuous measurements of

the thermal structure, data not shown, but mixing regime summarized in Table 3), before the ponds started to freeze.

Continuous CO<sub>2</sub> and DO measurements over a 6-d period in mid-July at the surface of BYL24, an IWT pond rich in vegetation (Fig. 8c), showed a clear diurnal pattern (Fig. 9a). Even though the highs and lows were not observed at the same time each day (CO<sub>2</sub> maximum occurred from 1 to 9 a.m., and the minimum from 6 to 9 p.m.), the pond still showed strong diurnal cycles in both gases, with DO inversely related to CO<sub>2</sub> ( $r^2 = -0.921$ ,  $p$  value < 0.001).

Despite the high ebullition fluxes measured from IWT ponds (CH<sub>4</sub> flux averages varied from 0.1 to 5.9 mmol m<sup>-2</sup> d<sup>-1</sup>, depending on pond and year, with a maximum of 31.8 mmol m<sup>-2</sup> d<sup>-1</sup>), CH<sub>4</sub> collected for <sup>14</sup>C analysis was modern in age (Fraction modern [Fm] > 1, with <sup>14</sup>C from mid-20<sup>th</sup> century atmospheric thermonuclear weapons tests; Table 5 and Fig. 5a). However, ponds with more stable shores (less

erosion, more vegetation) emitted CH<sub>4</sub> that was slightly more enriched in <sup>14</sup>C (BYL24, average Fm = 1.037 ± 0.005) compared to those presenting active shore erosion (BYL27, BYL117; average Fm = 1.011 ± 0.011). The same spatial trend was obtained for CO<sub>2</sub> (Fm = 0.991 vs 0.983 ± 0.024, respectively, for the pond with stable shores vs. ponds with active erosion). While the <sup>14</sup>CH<sub>4</sub> remained similar throughout the ice-free season, the <sup>14</sup>CO<sub>2</sub> changed over time, with slightly older CO<sub>2</sub> emitted in late June compared to early August (Fig. 6); thus, showing an opposite trend compared to the thermokarst lake. IWT ponds had the same range of δ<sup>13</sup>CO<sub>2</sub> values (−22‰ to −11‰) as the other water bodies studied on Bylot Island (Fig. 5d). However, δ<sup>13</sup>CH<sub>4</sub> values were higher, particularly for dissolved CH<sub>4</sub> (−62‰ to −40‰), with no clear difference between erosive and stable IWT ponds (Fig. 5b). While δ<sup>2</sup>H of dissolved CH<sub>4</sub> was similar to the other water bodies (−396‰ to −305‰), ebullition gas values were conspicuously low (−448‰ to −323‰).

### Coalescent polygonal ponds

During most of the open-water season, CP ponds were CO<sub>2</sub> sinks. The CO<sub>2</sub> uptake rate increased with time (on average from 2.5 mmol m<sup>−2</sup> d<sup>−1</sup> in late June to 4.1 mmol m<sup>−2</sup> d<sup>−1</sup> in late July), and then slowed in August with the onset of cooler and darker nights. The pattern was opposite for the CH<sub>4</sub> flux; it was highest in spring and decreased during summer (Fig. 4). Since there was no storage at the bottom of the water column of these well-mixed ponds, and because the autumnal fluxes were estimated using the same method as for stratified ponds, the presented values were similar to late summer fluxes (i.e., still negative in the case of CO<sub>2</sub>; Fig. 3). Ebullition contributed a larger fraction of total CH<sub>4</sub> emissions in CP ponds compared to the other water bodies, reaching 91% in spring (Fig. 4).

The majority of ebullition samples collected from two CP ponds showed a modern radiocarbon signature (i.e., after 1950; Table 5). The available data point suggest a seasonal trend, with CH<sub>4</sub> being slightly less enriched in <sup>14</sup>C in spring (i.e., a greater contribution of older carbon), and a rising trend in Fm throughout the open-water season (Fig. 6). Conversely, the emitted CO<sub>2</sub> was more enriched in <sup>14</sup>C in spring (younger than modern), with a decreasing trend towards the autumn, and centuries-old carbon emitted by the end of summer. In general, the radiocarbon age of DOC and dissolved CO<sub>2</sub> was modern (Table 5). Despite showing little variation in terms of GHG fluxes, CP ponds were characterized by highly variable stable isotope signatures (dissolved and ebullition δ<sup>13</sup>CO<sub>2</sub> values ranging from −22‰ to −0.1‰; Table 6 and Fig. 5d). There was a clear distinction between dissolved δ<sup>13</sup>CH<sub>4</sub> (−54‰ to −42‰) and ebullition δ<sup>13</sup>CH<sub>4</sub> (−71‰ to −52‰).

### Discussion

The four morphologically distinct water body types studied on Bylot Island showed different seasonal patterns in CO<sub>2</sub> and

CH<sub>4</sub> concentrations, fluxes, and isotopic signatures, partly dictated by their morphology and mixing regime. The biogeochemistry of Arctic lakes is expected to be quite different from their subarctic counterparts in terms of permafrost extent, parent material, history of past thaw events, and seasonality (Tank et al. 2020). The observed ranges for most part concur with previous studies, although comparative studies remain scarce in Arctic tundra regions. The studied polygonal landscape represents an Arctic wetland environment, characterized by numerous water bodies (Fig. 1), relatively lush tundra vegetation and organic-rich soils (Minke et al. 2007; Gauthier et al. 2011; Abnizova et al. 2012; Lara et al. 2015; Muster et al. 2017). Overall, the variability was quite large over a small area (1 km<sup>2</sup>); therefore, not taking into account these patterns can lead to large upscaling errors, and to misleading interpretations when comparing studies.

### Winter storage and spring flux

While the spring season is brief for lakes and ponds on Bylot Island (unfreezing or ice-out period lasts ~ 10 d for ponds and up to 3 weeks for lakes; Table 3), it is the period during which considerable amounts of GHG are emitted from these water bodies (Figs. 3, 4). For example, CP ponds more often showed positive CO<sub>2</sub> fluxes (i.e., represented a net source) as compared to the following summer period (net sink; Table S2). Also, most of the studied ponds experienced high ebullition rates during this period, with up to 52% of all CH<sub>4</sub> emitted during the open-water season occurring in spring, when normalized for the season lengths.

For lakes, between 40% and 80% (BYL66 and BYL36, respectively) of all annual CO<sub>2</sub> emissions occurred during the spring, but only 3% to 12% of annual CH<sub>4</sub> emissions. This can be related to the high CO<sub>2</sub> but relatively low CH<sub>4</sub> concentrations observed under the ice cover (Fig. 3). Such a discrepancy could be attributed to persistent methanotrophic activity in the water column during winter and spring, despite the low temperatures. This has been reported from boreal lakes where winter methanotrophy was found to be equally important to that of summer (Kankaala et al. 2006; Elder et al. 2019). The extent of methanotrophic oxidation affects the net CH<sub>4</sub> emissions from lakes and ponds; a better assessment of the importance of this mitigating effect and its response to changes in ice cover length, water temperature, mixing regime and oxygen level is therefore needed (Bartosiewicz et al. 2019; Woolway and Merchant 2019).

The presented GHG emission rates from lakes in spring may still be conservative for many reasons. Firstly, a portion of under-ice winter storage in lakes was likely in the form of gas pockets trapped under the ice cover, which rapidly escaped as soon as the ice started to break apart (Walter Anthony et al. 2010). Secondly, the GHG storage within the ice cover was likely underestimated as it was based on concentrations from the top portion of the ice cover (60 cm out of about 2 m of ice), while CH<sub>4</sub> concentrations in the ice has been shown

to increase with depth (Langer et al. 2015). Also, when conditions finally allowed ebullition flux measurements, a fraction of the gases trapped in the ice cover, water column or sediment pore water had likely already escaped. The discrepancy observed between dissolved GHG measured under the lake ice cover in early June and at the lake surface in early July (winter CO<sub>2</sub> concentration up to 14 times higher) highlights the importance of the spring flux, and underlines the need to develop better methods to capture this critical and challenging period. This was also highlighted by Jammot et al. (2015) who found that spring flux accounted for 53% of annual emission from a subarctic lake.

The CO<sub>2</sub> concentrations calculated in the ice cover (at 60 cm) were similar to July surface water concentrations in the IWT pond BYL27, but not in the CP pond BYL80 (Fig. 3). Similar concentrations may indicate the release of ice-trapped gases to the water column upon melting (and later its transfer to the atmosphere), while the early onset of photosynthetic activity could explain the difference observed in CP ponds. Microbial mats have indeed been observed to form on the ice surface soon after the ice started to melt (Fig. 8a,d). On the other hand, the early rise in CH<sub>4</sub> emissions from CP ponds was mainly through the ebullition pathway (91% of total spring flux). During this period, the ice was still present at the bottom; therefore, the emitted CH<sub>4</sub> originated from gases trapped in the ice since the previous autumn. The spring ebullition rate in CP ponds was three times higher than that in the early summer period (Fig. 4), with the flux decreasing as soon as ponds were free of ice (moment identified from thermistors placed in pond sediments).

In contrast to the other water body types, spring was not an exceptional period for IWT pond emissions, as we found relatively constant averaged CH<sub>4</sub> emissions from spring to the end of summer, close to 2 mmol m<sup>-2</sup> d<sup>-1</sup>. However, it is very likely that we missed sporadic bubbling events during the ice-melting period. Intense and sudden bubbling events lasting up to 20 min were observed several times (see the video presented in the data repository Prėskienis et al. 2020).

### Summer diffusive flux

The limnological summer, lasting about 6 weeks on Bylot Island, is the most widely studied period in the Arctic. This seasonal bias, mostly caused by logistical constraints, nevertheless allows a relatively well-documented comparison between studies. In general, our results fall within the range of CO<sub>2</sub> and CH<sub>4</sub> fluxes recorded from lakes and ponds across the Arctic (Table 1; see also Table 3 in Matveev et al. 2016, and Table 4 in Bouchard et al. 2015 for circumpolar comparisons), underlining the importance of including the tundra biome in global estimates (Wik et al. 2016a). The highest CO<sub>2</sub> flux measured on Bylot are from IWT ponds, and particularly from ponds subject to active erosion (e.g., on average 53 mmol m<sup>-2</sup> d<sup>-1</sup> over the late summer period for BYL27, maximum recorded flux of 118 mmol m<sup>-2</sup> d<sup>-1</sup>). These values are among

the highest CO<sub>2</sub> fluxes reported for tundra lakes (Table 1). However, higher CO<sub>2</sub> diffusive fluxes were reported from subarctic thermokarst lakes (> 350 mmol m<sup>-2</sup> d<sup>-1</sup> from yedoma landscape in Eastern Siberia, Hughes-Allen et al. (2020); 242 mmol m<sup>-2</sup> d<sup>-1</sup> from Quebec palsas peatlands, Matveev et al. 2016).

IWT ponds are also large CH<sub>4</sub> emitters (late summer average 1.8 mmol m<sup>-2</sup> d<sup>-1</sup> for BYL27, maximum recorded flux of 5 mmol m<sup>-2</sup> d<sup>-1</sup> from BYL67), with high diffusive fluxes observed throughout the stratified summer period (Fig. 4). These high fluxes suggest that respiration and methanogenesis were relatively important in the warmer and organic-rich epilimnetic water column and littoral sediments, considering that pelagic and littoral zones are in close proximity for water bodies of a few square meters (the pelagic zone in IWT ponds being defined as the water column showing a persistent stratification with an epilimnion and hypolimnion, as opposed to the littoral zone that is shallower than the epilimnion). Elevated diffusive flux under stratified conditions can also result from the upwelling of deeper, GHG-enriched waters through partial mixing caused by wind and especially by nocturnal cooling in sheltered IWT ponds (Walter Anthony and MacIntyre 2016, MacIntyre et al. 2018; see also section below on diurnal cycles). However, these mixing events were apparently not long or deep enough to vent out all accumulated gases until autumnal cooling occurs, since the hypolimnetic concentrations remained high during summer (ranging from 25 to 233 μM in different IWT ponds; Fig. 7). In other tundra regions, higher CH<sub>4</sub> fluxes were mainly reported for systems studied late in summer (August; Sebachner et al. 1986), potentially during the mixing period when stored GHG are released, or at sites close to the tree-line, receiving DOM inputs from large river systems (Bartlett et al. 1992; Cunada et al. 2018).

CP ponds remained CO<sub>2</sub> sinks throughout the summer. This likely reflects the particularly efficient photosynthetic uptake by microbial mats in these water bodies, combined with an efficient transfer of CO<sub>2</sub> from the atmosphere as the water column is permanently mixed in these ponds. Their shallow, well-mixed, and transparent water column (low turbidity and CDOM due to negligible levels of shore erosion; Table 2) creates an environment well suited for the establishment of thick benthic cyanobacterial mats, dominated by *Oscillatoria* sp. (Vėzina and Vincent 1997; Negandhi et al. 2014). Continuous daylight during early summer allows active photosynthesis even at night (although limited by lower irradiance), making these water bodies almost constant CO<sub>2</sub> sinks (Fig. 4).

The highest uptake rates of CO<sub>2</sub> recorded at Bylot were measured in CP ponds; they were also notably higher than other reported values in the Arctic (Table 1). Moreover, these uptake rates were potentially underestimated because we did not account for the chemical enhancement of CO<sub>2</sub> uptake, particularly induced when pH rises above 9.5 under low wind conditions (Hoover and Berkshire 1969). This effect has recently been reported to be strong during summer for

shallow, high-pH (generally > 9) “*alas*” lakes typical of yedoma landscapes in eastern Siberia (Hughes-Allen et al. 2020). The pH of Bylot CP ponds rarely reached such high values (Table 2), and we estimated that the chemical enhancement varied between 1 and 3.6 (on average 1.2,  $N = 142$ ). Therefore, the CO<sub>2</sub> uptake in these ponds may have been about 20% higher than reported, a factor that should be taken into account.

### Summer ebullition flux

Methane ebullition rates obtained on Bylot Island were comparable to values reported for tundra lakes on the Alaskan North Slope (Table 1). Although the contribution of ebullition to total CH<sub>4</sub> emissions was highly variable and strongly dependent on water body morphology and season (varying from 0.1% to 99%), it remains an important emission pathway for Bylot lakes and ponds (global average of 52% for water bodies presented in Fig. 4). When factoring in the global warming potential of CH<sub>4</sub> over 100 years (GWP<sub>100</sub> index, in CO<sub>2</sub>-equivalent; Table 4), ebullition contributed 60% to 95% of total emissions, with the exception of kettle lakes (2–15% of GWP<sub>100</sub>) and ponds with thick brown moss coverage (such as IWT pond BYL24 and CP pond BYL30).

We never observed point-source ebullition from Bylot Island water bodies—except when escaping from the melting and cracking ice in ponds at the end of June—nor did we observe large bubble clusters on the ice transects carried out in the first week of June. Therefore, we suspect that background ebullition (as defined by Walter et al. 2006) is the main mode of bubble evasion at the studied site. The <sup>13</sup>C isotopic fractionation factor between CH<sub>4</sub> and CO<sub>2</sub> ( $\alpha_c$ ) in the collected samples (mean value of 1.048) was similar to the background ebullition signature obtained from lakes in West Siberian tundra (Walter et al. 2008). Since background ebullition is typically less spatially variable, it makes the small area coverage of the ebullition funnels (1–2 in ponds, 4 in lakes) less of an issue. Nevertheless, we cannot exclude the possibility that point-source events occurred, making our estimates conservative (Wik et al. 2016b).

In general, kettle lakes showed the lowest ebullition rates of the study site; they are more transparent (lower DOM) and less productive (lower nutrients) than other water bodies. The majority of ebullition gases were collected from the littoral zones, where benthic vegetation was observed. Ebullition rates decreased by three orders of magnitude when moving to the pelagic zone, where less bubbles are expected to reach the surface due to the longer travel path (11 m) and greater hydrostatic pressure (Bastviken et al. 2004; McGinnis et al. 2006), especially for background ebullition (smaller bubbles). Glacial and post-glacial lakes (which include kettle lakes) are known to be small emitters per m<sup>2</sup>, but as they are abundant north of ~ 50°N (79% of total lakes and ponds by area), they are considered to be important CH<sub>4</sub> contributors globally (about 50% of annual CH<sub>4</sub> emissions north of 50°N as estimated by Wik

et al. 2016a). The shallow thermokarst lake BYL123 and the littoral zone of BYL66 presented similar ebullition rates as the kettle lakes, while the deep zone of thermokarst Lake BYL66 was characterized by 10 times higher rates. These shallow zones lacked a substantial gyttja layer, and are directly underlain by terrestrial peaty silt, while the deep basin of BYL66 is covered by a ~ 10 cm layer of gyttja (Bouchard et al. 2020) underlain by an organic-rich talik, fuelling CH<sub>4</sub> production (more details below in section “The carbon source of emitted GHG”).

Overall, both CP and IWT ponds experienced similar ebullition rates (Table 4). However, while CP ponds maintained rather constant rates every year, IWT ponds showed much higher interannual variability. For example, Pond BYL27 emitted 17.4 mmol CH<sub>4</sub> m<sup>-2</sup> d<sup>-1</sup> at mid-July in 2014, while in 2015 flux was barely reaching 0.2 mmol CH<sub>4</sub> m<sup>-2</sup> d<sup>-1</sup> over the same period. This is most likely due to the complex bathymetry of IWT ponds and their discontinuous and erratic shore erosion events, whereas methanogens in CP ponds are likely supplied by more constant benthic primary production. The observed difference may be further magnified by the depth constraint on funnel deployment; to avoid sediment disturbance, only sites deeper than 40 cm were selected. For CP ponds with a relatively flat bottom, funnels were likely a better representation of their ebullition rates, whereas for IWT ponds, funnel deployment was biased toward deeper sections which thaw later and maintain colder bottom sediments, thus likely underestimating total ebullition. Considering the large amount of small and shallow water bodies in polygonal landscapes, and that shallow waterlogged permafrost areas are often reported as important CH<sub>4</sub> emitters (e.g., Olefeldt et al. 2013), other methods will have to be applied to assess the carbon footprint of these systems at the landscape scale, for example using eddy co-variance flux towers (Abnizova et al. 2012; Sturtevant and Oechel 2013).

### Summer storage flux

Both the kettle lakes and the IWT ponds became stratified during the summer, and accumulated CO<sub>2</sub> and CH<sub>4</sub> in their hypolimnion. However, only the hypolimnion volume of IWT ponds was large enough (e.g., 15% of total volume for BYL27) to generate a significant increase in GHG flux during the autumnal mixing period (3.1 × larger CO<sub>2</sub> flux and 8.3 × larger CH<sub>4</sub> flux for BYL27). Summer storage flux in shallow ponds remains overlooked by most studies, perhaps because these systems are not generally considered as stratified.

As expected, under the steady turbulent mixing occurring in the thermokarst lakes and CP ponds, venting of GHG occurred throughout the summer, and thus summer storage fluxes estimated for these water bodies were comparable to summer fluxes (Fig. 4). However, autumnal fluxes comprise not only the venting of GHG stored in the hypolimnion (summer storage flux), but also autumnal production in the water column and sediments (not measured in the present study),

which is expected to be significant considering the time lag before bottom waters and sediments cool down. Moreover, the estimated summer storage fluxes did not include ebullition, which has been shown to continue year-round in thermokarst lakes of Alaska and Siberia (Walter Anthony et al. 2010), and even peak in October–January in deeper lakes (Zimov et al. 1997). Therefore, our flux estimates for the autumnal period are conservative.

### Diurnal cycles in GHG concentrations

The diurnal cycles obtained with the continuous measuring system installed in IWT pond BYL24 indicate that surface  $\text{CO}_2$  peaked in the morning and DO peaked in the evening (Fig. 9a), even though the pond maintained a stratified water column for most of the open-water season, with significant temperature differences between surface and bottom waters (about  $10^\circ\text{C}$  in July). Such opposing cycles in  $\text{CO}_2$  and DO may have resulted from (1) the balance between night-time respiration and day-time photosynthesis, and (2) a diurnal pattern in mixing regime. Surface waters cooling at night create small eddies, slowly mixing with the deeper, GHG-enriched, water mass, thus creating a potentially important escape pathway (Walter Anthony and MacIntyre 2016).

CP ponds were also expected to show strong diurnal cycles in gas concentrations, but primary production by microbial mats maintained  $\text{CO}_2$  concentrations largely below atmospheric levels and below the detection limit for the continuous gas monitoring system. On the other hand, the discrete data collected from Pond BYL80 over many days in July, when pooled, showed a significant rising trend in dissolved  $\text{CH}_4$  at

the surface from about 3:00 a.m. to midnight (Fig. 9b). This rise in  $\text{CH}_4$  concentration potentially resulted from two concurrent processes linked to daily variations in sunlight: (1) increasing photosynthetic activity by benthic mats providing labile autochthonous matter to methanogens (Berg et al. 2014; West et al. 2015), and (2) rising light inhibition of methanotrophs, as shown in temperate lakes by Thottathil et al. (2018). We did not observe such trend in IWT ponds, potentially because they are light limited (higher CDOM and TSS) and highly stratified; thus, surface  $\text{CH}_4$  concentrations are more likely to be controlled by a partial mixing with hypolimnetic waters rather than by the production-consumption balance.

### Methane production and oxidation

The stable isotopic composition of  $\text{CH}_4$  (dissolved in surface waters or emitted through ebullition) as well as the  $^{13}\text{C}$  isotopic fractionation factor between  $\text{CH}_4$  and  $\text{CO}_2$  ( $\alpha_c = 1.040\text{--}1.055$ ) both imply that acetoclastic methanogenesis is the major  $\text{CH}_4$  production pathway in Bylot ponds and lakes (Fig. 10; Whiticar et al. 1986). However, as the majority of stable isotope data were collected in July, it is possible that the lower availability of labile organic compounds in earlier or later months might switch prevailing methanogenesis to hydrogenotrophy ( $\text{CO}_2$  reducing; Alstad and Whiticar 2011). The hydrogenotrophic methanogens were indeed identified as equally abundant in genomic analyses of pond sediments at the study site (Negandhi et al. 2013).

A portion of produced  $\text{CH}_4$  can be consumed by methanotrophs before being emitted to the atmosphere, and an active methanotrophy has been associated with brown mosses

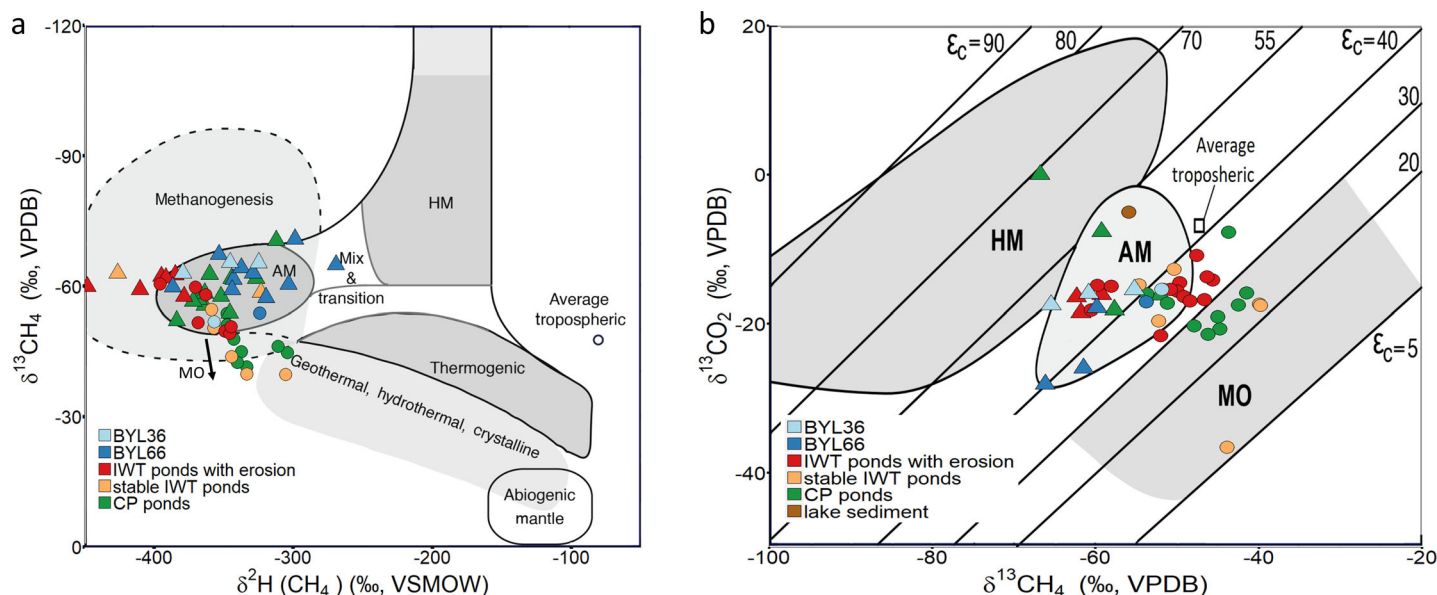


**Fig. 10.** (a) Carbon ( $\delta^{13}\text{C}$ ) and hydrogen ( $\delta^2\text{H}$ ) isotope composition of  $\text{CH}_4$  dissolved in surface water (circles) or emitted through ebullition (triangles) for coalescent ponds (CP), ice-wedge trough ponds (IWT), kettle lake (BYL36), thermokarst lake (BYL66), and BYL66 sediment pore water (lake sediment), after Whiticar et al. (1986). (b) Carbon isotope composition ( $\delta^{13}\text{C}$ ) of  $\text{CH}_4$  (x-axis) and  $\text{CO}_2$  (y-axis) from the same samples. AM, acetoclastic methanogenesis; HM, hydrogenotrophic methanogenesis; MO, methanotrophy.

in tundra ponds of the Lena Delta (Liebner et al. 2011). Brown mosses are also abundant in Bylot, in CP ponds and IWT ponds with stable shores, where the majority of dissolved gas isotopic data clearly showed a high level of CH<sub>4</sub> oxidation (based on enriched  $\delta^{13}\text{C}$  values of CH<sub>4</sub> and depleted values for CO<sub>2</sub>; Figs. 5b,d, 10) compared to the IWT ponds with erosive shores (limited primary production). Therefore, this mitigating effect on CH<sub>4</sub> emission might not operate efficiently in erosive IWT ponds that are likely to become more abundant on polygonal landscapes affected by permafrost thawing.

Dissolved CH<sub>4</sub> concentration in the CP pond BYL80 was strongly correlated with water temperature ( $p$  value = 0.007;  $r^2 = 0.724$ ; data averaged over 5-d intervals over the open-water season), but the ebullition rates were not ( $p$  value = 0.212;  $r^2 = 0.007$ ; temperature averaged over each funnel accumulation period). This may imply that even though CH<sub>4</sub> production is temperature sensitive (e.g., Thanh-Duc et al. 2010; Wik et al. 2014; Yvon-Durocher et al. 2014), its evasion through ebullition is controlled by other factors. Without direct investigations of production (and consumption) rates in response to temperature and substrate availability, it is difficult to determine if CH<sub>4</sub> emissions will increase or decrease with longer and warmer summers as these conditions will also affect primary producers.

### The carbon source of emitted GHG

Most studies presenting radiocarbon dates on GHG evading from Arctic lakes have been conducted in yedoma regions, where carbon of pleistocene age was shown to be used by methanogens (e.g., Zimov et al. 1997; Walter et al. 2008). More recently, studies on thermokarst lakes from boreal Alaska on non-yedoma deposits showed that ebullition GHG were produced from carbon pools of the last millennia (2330 YBP for CH<sub>4</sub>, 585 YBP for CO<sub>2</sub>; Elder et al. 2019), and that dissolved gases in these lakes had a relatively recent carbon signature (mostly modern, but up to 3300 YBP for CH<sub>4</sub> and 1590 YBP for CO<sub>2</sub>; Elder et al. 2018, 2019). This is consistent with what we observed on Bylot Island, where emissions primarily originated from recently fixed carbon (Table 5).

At one extreme, CP ponds, colonized by mosses and thick cyanobacterial mats and with no visible erosion, emit GHG principally deriving from recent primary production (averaged Fm 1.03, and enriched  $\delta^{13}\text{C}$ , Table 6; Fig. 5d). Although most dates obtained from ponds were modern, ebullition CO<sub>2</sub> became slightly older (from decades to 1220 YBP) in CP ponds as summer progressed and the thaw front deepened. Methane showed the opposite trend, with a slightly older carbon (within the last century) during the ice-out compared to late summer (Fig. 6; Table 5). With CP ponds covered by actively photosynthesizing benthic mats, freshly produced organic matter becomes more available to methanogens as summer progresses. The methanogens may preferentially use this readily labile material as their metabolism is less efficient compared to aerobic microbes (Canfield et al. 2005). The relatively

older carbon of CO<sub>2</sub> later in season may be linked to the bacterial consumption of terrestrial organic matter leaching in pore water from deeper soils, and laterally transferred to ponds, depending on rain patterns and local topography.

In IWT ponds, the radiocarbon ages remained stable over time (Fig. 6), especially for CH<sub>4</sub>, suggesting limited seasonal changes in the source of carbon exploited by microorganisms. On the other hand, carbon of CO<sub>2</sub>, CH<sub>4</sub> and DOC in IWT ponds featuring actively eroding shores (BYL27 and BYL117) was relatively more <sup>14</sup>C-depleted (average Fm < 1) compared to CP ponds and IWT pond colonized by primary producers (average Fm > 1; Fig. 5b,d; Table 5). These eroding ponds contain less autochthonous organic matter as their unstable shores and turbid waters are less favorable to primary producers. Furthermore, they receive a significant amount of <sup>14</sup>C-depleted carbon from falling thawed peat (dated to 2210–2535 YBP at the base of the active layer). However, the contribution of this older carbon to GHG production may not be evident if its fractional contribution is small, because it can be strongly diluted by the presence of modern carbon, as suggested by Drake et al. (2018), who studied an Arctic fluvial network. Therefore, the mobilization and microbial utilization of old carbon in the system can be hidden. Further constraining the role of old carbon in these ponds requires more specific approaches, such as the compound-specific radiocarbon analysis of lignin phenols as applied by Feng et al. (2017), or a more detailed analysis of isotopic composition, such as the Keeling plot approach (Pataki et al. 2003).

The only sampled water body constantly emitting older carbon was the thermokarst lake BYL66. Methane emitted from the pelagic (deepest) zone of this lake was significantly more <sup>14</sup>C-depleted (up to 3405 YBP for ebullition CH<sub>4</sub>) compared with the littoral zone (1500–2775 YBP). Siberian and Alaskan thermokarst lakes showed the opposite pattern, where the littoral zones (thermokarst margins) presented the oldest CH<sub>4</sub> signatures (and highest ebullition rates; Walter et al. 2006; Walter Anthony et al. 2016). However, these yedoma lakes are located within thicker unconsolidated sediments that actively erode once the ice-rich permafrost thaws. In the case of the thermokarst lake on Bylot Island, younger CH<sub>4</sub> emitted from the littoral zone may be explained by two factors: (1) the active layer underneath the littoral zone is limited in depth as the water column in this section of the lake refreezes to the bottom each winter, restricting the methanogens to carbon from shallower (younger) peat and freshly deposited autochthonous OM, and (2) lake expansion to this area is relatively recent, hence the submerged peat-rich terrace was formed more recently than the one underlying the deep basin (Bouchard et al. 2020). The deep basin of BYL66 (~ 4 m depth) maintains a layer of water throughout the winter, creating a talik underneath, thus allowing methanogens to access deeper horizons. The oldest age obtained on BYL66 gyttja was 2073 YBP (Bouchard et al. 2020), while the age of ebullition CH<sub>4</sub> was older (Table 5), indicating that the underlying peat layer was being used as a carbon source.

Ebullition CO<sub>2</sub> from Bylot Island lakes showed younger ages than CH<sub>4</sub>, as was also found in Alaskan thermokarst lakes (Elder et al. 2019). However, ponds showed the opposite trend (generally slightly older CO<sub>2</sub> compared to CH<sub>4</sub>; Fig. 5c), potentially suggesting a decoupled carbon cycle between pathways producing CH<sub>4</sub> and CO<sub>2</sub> in sediments. In lakes, CH<sub>4</sub> can be produced from deeper (older) horizons (in taliks), while access to older organic matter is limited in ponds (no talik) and fresh organic matter is more readily available from benthic mats, brown mosses and aquatic plants.

## Conclusions

Water body morphology significantly influenced the CO<sub>2</sub> and CH<sub>4</sub> flux patterns observed during the open-water season on this typical lowland tundra polygonal landscape. While kettle lakes experienced their highest gas fluxes early in the season, the studied thermokarst lake maintained relatively high emissions during the whole open-water season and was an important emitter of millennial-aged carbon. Emissions from IWT ponds increased from spring to autumn, whereas CP ponds had their maximum CH<sub>4</sub> flux in spring and maintained a relatively high flux throughout the summer, whilst being constant CO<sub>2</sub> sinks. Ponds are a particularly critical component of GHG emissions in this permafrost landscape, as they present the highest warming potential index per area, and their global areal coverage is likely to expand in the near future. They are particularly responsive to variations in primary production, precipitation regime and erosion events. With increasing precipitation and shortening winters, conditions can favor both the growth of primary producers and the intensification of carbon-rich permafrost erosion. Therefore, although these ponds presently emit century-old to modern <sup>14</sup>C, further studies will need to rely on radiocarbon dating and stable isotopes to track future changes in the predominantly mineralized carbon source. Palaeoclimatic studies are also required to determine if present-day thermokarst erosion has accelerated during the Anthropocene, which is a condition for considering Holocene carbon mineralization as part of the positive feedback mechanism. Although studying ponds is challenging due to their small size, complex bathymetry and mixing regime, variable seasonal patterns and sensitivity to environmental changes, they must be considered in assessing the effects of permafrost thaw on the global carbon cycle.

## References

Abnizova, A., J. Siemens, M. Langer, and J. Boike. 2012. Small ponds with major impact: The relevance of ponds and lakes in permafrost landscapes to carbon dioxide emissions. *Global Biogeochem. Cycles* **26**. doi:10.1029/2011GB004237

Ai, G., J. Zhu, X. Dong, and T. Sun. 2013. Simultaneous characterization of methane and carbon dioxide produced by

cultured methanogens using gas chromatography/isotope ratio mass spectrometry and gas chromatography/mass spectrometry. *Rapid Commun. Mass Spectrom.* **27**: 1935–1944. doi:10.1002/rcm.6651

Alstad, K. P., and M. J. Whiticar. 2011. Carbon and hydrogen isotope ratio characterization of methane dynamics for Fluxnet Peatland Ecosystems. *Org. Geochem.* **42**: 548–558. doi:10.1016/j.orggeochem.2011.03.004

Bartlett, K. B., P. M. Crill, R. L. Sass, R. C. Harriss, and N. B. Dise. 1992. Methane emissions from tundra environments in the Yukon-Kuskokwim delta, Alaska. *J. Geophys. Res.* **97**: 16645–16660. doi:10.1029/91JD0061

Bartosiewicz, M., A. Przytulska, J. F. Lapierre, I. Laurion, M. F. Lehmann, and R. Maranger. 2019. Hot tops, cold bottoms: Synergistic climate warming and shielding effects increase carbon burial in lakes. *Limnol. Oceanogr.* **4**: 132–144. doi:10.1002/lol2.10117

Bastien, J., J.L. Frėchette, and R.H. Hesslein. 2008. Continuous greenhouse gas monitoring system—operating manual. Report prepared by Environnement Illimitė Inc. for Manitoba Hydro and Hydro-Quėbec.

Bastviken, D., J. Cole, M. Pace, and L. Tranvik. 2004. Methane emissions from lakes: Dependence of lake characteristics, two regional assessments, and global estimate. *Global Biogeochem. Cycles* **18**. doi:10.1029/2004GB002238

Bell, T., and T. M. Brown. 2018. From science to policy in the Eastern Canadian Arctic: An integrated regional impact study (IRIS) of climate change and modernization. Quebec City: ArcticNet.

Berg, A., P. Lindblad, and B. H. Svensson. 2014. Cyanobacteria as a source of hydrogen for methane formation. *World J. Microbiol. Biotechnol.* **30**: 539–545. doi:10.1007/s11274-013-1463-5

Bintanja, R., and F. Krikken. 2016. Magnitude and pattern of Arctic warming governed by the seasonality of radiative forcing. *Nat. Sci. Rep.* **6**: 38287. doi:10.1038/srep38287

Biskaborn, B. K., and others. 2019. Permafrost is warming at a global scale. *Nat. Commun.* **10**, 264, doi:10.1038/s41467-018-08240-4

Bogard, M. J., and others. 2019. Negligible cycling of terrestrial carbon in many lakes of the arid circumpolar landscape. *Nat. Geosci.* **12**: 180–118. doi:10.1038/s41561-019-0299-5

Bokhorst, S., and others. 2016. Changing Arctic snow cover: A review of recent developments and assessment of future needs for observations, modelling, and impacts. *Ambio* **45**: 516–537, doi:10.1007/s13280-016-0770-0

Breton, J., C. Valliėres, and I. Laurion. 2009. Limnological properties of permafrost thaw ponds in Northeastern Canada. *Can. J. Fish. Aquat. Sci.* **66**: 1635–1648. doi:10.1139/F09-108

Buell, M.C. 2015. CO<sub>2</sub> dynamics of tundra ponds in the low-Arctic, Northwest Territories, Canada. MS Thesis. Trent Univ..

Bouchard, F., I. Laurion, V. Prėskienis, D. Fortier, X. Xu, and M. J. Whiticar. 2015. Modern to millennium-old

- greenhouse gases emitted from ponds and lakes of the Eastern Canadian Arctic (Bylot Island, Nunavut). *Biogeosciences* **12**: 7279–7298. doi:[10.5194/bg-12-7279-2015](https://doi.org/10.5194/bg-12-7279-2015)
- Bouchard, F., D. Fortier, M. Paquette, V. Boucher, R. Pienitz, and I. Laurion. 2020. Thermokarst lake inception and development in syngenetic ice-wedge polygon terrain during a cooling climatic trend, Bylot Island (Nunavut), eastern Canadian Arctic. *The Cryosphere* **14**: 2607–2627. doi:[10.5194/tc-14-2607-2020](https://doi.org/10.5194/tc-14-2607-2020)
- Canfield, D. E., B. Thamdrup, and E. Kristensen. 2005. *Aquatic geomicrobiology*, 2nd ed. Elsevier Academic Press.
- Centre for northern studies (CEN). 2020. Climate station data from Bylot Island in Nunavut, Canada, v. 1.11 (1992–2019). Nordicana **D2**. doi:[10.5885/45039SL-EE76C1BDAADC4890](https://doi.org/10.5885/45039SL-EE76C1BDAADC4890)
- Cunada, C. L., L. F. W. Lesack, and S. E. Tank. 2018. Seasonal dynamics of dissolved methane in lakes of the Mackenzie Delta and the role of carbon substrate quality. *Eur. J. Vasc. Endovasc. Surg.* **123**: 591–609. doi:[10.1002/2017JG004047](https://doi.org/10.1002/2017JG004047)
- Dean, J. F., and others. 2018. Abundant pre-industrial carbon detected in Canadian Arctic headwaters: implications for the permafrost carbon feedback. *Environ. Res. Lett.* **13**: 034024. doi:[10.1088/1748-9326/aaa1fe](https://doi.org/10.1088/1748-9326/aaa1fe)
- Dlugokencky E. and P. Tans. 2017. Globally averaged marine surface annual mean data. Earth System Research Laboratory, National Atmospheric and Ocean Administration. Available from [www.esrl.noaa.gov/gmd/ccgg/trends/gl\\_data.html](http://www.esrl.noaa.gov/gmd/ccgg/trends/gl_data.html)
- Drake, T. W., F. Guillemette, J. D. Hemingway, J. P. Chanton, D. C. Podgorsky, N. S. Zimov, and R. G. M. Spencer. 2018. The ephemeral signature of permafrost carbon in an Arctic fluvial network. *Eur. J. Vasc. Endovasc. Surg.* **123**: 1475–1485. doi:[10.1029/2017JG004311](https://doi.org/10.1029/2017JG004311)
- Duclos, I., E. Lévesque, D. Gratton, and P. A. Bordeleau. 2006. Vegetation mapping of Bylot Island and Sirmilik National Park: Final report. Parks Canada.
- Elder, C. D., and others. 2018. Greenhouse gas emissions from diverse Arctic Alaskan lakes are dominated by young carbon. *Nat. Clim. Change* **8**: 166–171. doi:[10.1038/s41558-017-0066-9](https://doi.org/10.1038/s41558-017-0066-9)
- Elder, C. D., M. Schweiger, B. Lam, E. D. Crook, X. Xu, J. Walker, K. M. Walter Anthony, and C. I. Czimczik. 2019. Seasonal sources of whole-lake CH<sub>4</sub> and CO<sub>2</sub> emissions from Interior Alaskan thermokarst lakes. *Eur. J. Vasc. Endovasc. Surg.* **124**: 1209–1229. doi:[10.1029/2018JG004735](https://doi.org/10.1029/2018JG004735)
- Elder, C. D., D. R. Thompson, A. K. Thorpe, P. Hanke, K. M. Walter Anthony, and C. E. Miller. 2020. Airborne mapping reveals emergent power law of Arctic methane emissions. *Geophys. Res. Lett.* **47**: e2019GL085707. doi:[10.1029/2019GL085707](https://doi.org/10.1029/2019GL085707)
- Ellis, C. J., L. Rochefort, G. Gauthier, and R. Pienitz. 2008. Paleocological evidence for transitions between contrasting landforms in a polygon-patterned High Arctic wetland. *Arct. Antarct. Alp. Res.* **40**: 624–637. doi:[10.1657/1523-0430\(07-059\)\[ELLIS\]2.0.CO;2](https://doi.org/10.1657/1523-0430(07-059)[ELLIS]2.0.CO;2)
- Emmerton C. A., V. L. St. Louis, I. Lehnerr, J. A. Graydon, J. L. Kirk, and K. J. Rondeau. 2016. The importance of freshwater systems to the net atmospheric exchange of carbon dioxide and methane with a rapidly changing high Arctic watershed. *Biogeosciences* **13**: 5849–5863. doi:[10.5194/bg-13-5849-2016](https://doi.org/10.5194/bg-13-5849-2016)
- Feng, X., J. E. Vonk, C. Griffin, N. Zimov, D. B. Montluçon, L. Wacker, and T. I. Eglinton. 2017. <sup>14</sup>C variation of dissolved lignin in Arctic river systems. *ACS Earth Space Chem.* **1**: 334–344. doi:[10.1021/acsearthspacechem.7b00055](https://doi.org/10.1021/acsearthspacechem.7b00055)
- Fortier, D., and M. Allard. 2004. Late Holocene syngenetic ice-wedge polygons development, Bylot Island. *Can. J. Earth Sci.* **41**: 997–1012. doi:[10.1139/e04-031](https://doi.org/10.1139/e04-031)
- Fortier, D., M. Allard, and F. Pivot. 2006. A late-Holocene record of loess deposition in ice-wedge polygons reflecting wind activity and ground moisture conditions, Bylot Island, eastern Canadian Arctic. *Holocene* **16**: 635–646. doi:[10.1191/0959683606hl960rp](https://doi.org/10.1191/0959683606hl960rp)
- Garnett, M. H., K. J. Dinsmore, and M. F. Billett. 2012. Annual variability in the radiocarbon age and source of dissolved CO<sub>2</sub> in a peatland stream. *Sci. Total Environ.* **427–428**: 277–285. doi:[10.1016/j.scitotenv.2012.03.087](https://doi.org/10.1016/j.scitotenv.2012.03.087)
- Garnett, M. H., P. Guilliver, and M. F. Billett. 2016a. A rapid method to collect methane from peatland streams for radiocarbon analysis. *Ecohydrology* **9**: 113–121. doi:[10.1002/eco.1617](https://doi.org/10.1002/eco.1617)
- Garnett, M. H., M. F. Billett, P. Guilliver, and J. F. Dean. 2016b. A new field approach for the collection of samples for aquatic <sup>14</sup>CO<sub>2</sub> analysis using headspace equilibration and molecular sieve traps: the super headspace method. *Ecohydrology* **9**: 1630–1638. doi:[10.1002/eco.1754](https://doi.org/10.1002/eco.1754)
- Gauthier, G., D. Berteaux, J. Bėty, A. Tarroux, J. F. Therrien, L. McKinnon, P. Legagneux, and M. C. Cadieux. 2011. The tundra food web of Bylot Island in a changing climate and the role of exchanges between ecosystems. *Écoscience* **18**: 223–235. doi:[10.2980/18-3-3453](https://doi.org/10.2980/18-3-3453)
- Golubyatnikov, L. L., and V. S. Kazantsev. 2013. Contribution of Tundra Lakes in Western Siberia to the Atmospheric Methane Budget. *Izvestiya Atmos. Ocean. Phys.* **49**: 395–403. doi:[10.1134/S000143381304004X](https://doi.org/10.1134/S000143381304004X)
- Grosse, G., B. Jones, and C. Arp. 2013. Thermokarst lakes, drainage, and drained basins, p. 325–353. *In* J. F. Shroder, R. Giardino, and J. Harbor [eds.], *Treatise on geomorphology*. Vol 8: Glacial and periglacial geomorphology. Academic.
- Hesslein, R. H., J. W. M. Rudd, C. A. Kelly, P. Ramlal, and K. A. Hallard. 1991. Carbon dioxide pressure in surface waters of Canadian lakes, p. 413–431. *In* S. C. Wilhelms and J. S. Gulliver [eds.], *Air–water mass transfer*. American Society of Civil Engineers.
- Holgerson, M. A., and P. A. Raymond. 2016. Large contribution to inland water CO<sub>2</sub> and CH<sub>4</sub> emissions from very small ponds. *Nat. Geosci.* **9**: 222–226. doi:[10.1038/NGEO2654](https://doi.org/10.1038/NGEO2654)

- Hoover, T. E., and D. C. Berkshire. 1969. Effects of hydration on carbon dioxide exchange across an air-water interface. *J. Geophys. Res.* **92**: 1937–1949.
- Hugelius, G., et al. 2014. Estimated stocks of circumpolar permafrost carbon with quantified uncertainty ranges and identified data gaps. *Biogeosciences* **11**: 6573–6593, doi:10.5194/bg-11-6573-2014
- Hughes-Allen, L., F. Bouchard, I. Laurion, A. Sėjournė, C. Marlin, C. Hattė, F. Costard, A. Fedorov, and A. Desyatkin. 2020. Seasonal patterns in greenhouse gas emissions from thermokarst lakes in Central Yakutia (Eastern Siberia). *Limnol. Oceanogr.* in press. <https://www.doi.org/10.1002/lno.11665>
- Jammet, M., P. Crill, S. Dengel, and T. Friborg. 2015. Large methane emissions from a subarctic lake during spring thaw: Mechanisms and landscape significance. *Eur. J. Vasc. Endovasc. Surg.* **120**: 2289–2305. doi:10.1002/2015JG003137
- Kankaala, P., J. Huotari, E. Peltomaa, T. Saloranta, and A. Ojala. 2006. Methanotrophic activity in relation to methane efflux and total heterotrophic bacterial production in a stratified, humic, boreal lake. *Limnol. Oceanogr.* **51**: 1195–1204. doi:10.4319/lno.2006.51.2.1195
- Kinnaman, F. S., D. L. Valentine, and S. C. Tyler. 2007. Carbon and hydrogen isotope fractionation associated with the aerobic microbial oxidation of methane, ethane, propane and butane. *Geochim. Cosmochim. Acta* **71**: 271–283. doi:10.1016/j.gca.2006.09.007
- Klassen, R. A. 1993. Quaternary geology and glacial history of Bylot Island, Northwest Territories. *Geol. Survey Can. Mem.* 429. doi:10.4095/183984.
- Kling, G. W., G. W. Kipphut, and M. C. Miller. 1992. The flux of CO<sub>2</sub> and CH<sub>4</sub> from lakes and rivers in arctic Alaska. *Hydrobiologia* **240**: 23–36. doi:10.1007/bf00013449
- Kosten, S., F. Roland, D. M. L. Da Motta Marques, E. H. Van Nes, N. Mazzeo, L. d. S. L. Sternberg, M. Scheffer, and J. J. Cole. 2010. Climate-dependent CO<sub>2</sub> emissions from lakes. *Glob. Biogeochem. Cycles* **24**: GB2007. doi:10.1029/2009GB003618
- Langer, M. S. W., K. A. W. Anthony, K. Wischnewski, and J. Boike. 2015. Frozen ponds: production and storage of methane during the Arctic winter in a lowland tundra landscape in northern Siberia, Lena River delta. *Biogeosciences* **12**: 977–990. doi:10.5194/bg-12-977-2015
- Lara, M. J., and others. 2015. Polygonal tundra geomorphological change in response to warming alters future CO<sub>2</sub> and CH<sub>4</sub> flux on the Barrow Peninsula. *Global Change Biol.* **21**: 1634–1651. doi:10.1111/gcb.12757
- Laurion, I., W. F. Vincent, S. MacIntyre, L. Retamal, C. Dupont, P. Francus, and R. Pienitz. 2010. Variability in greenhouse gas emissions from permafrost thaw ponds. *Limnol. Oceanogr.* **55**: 115–133. doi:10.4319/lno.2010.55.1.0115
- Liebner, S., J. Zeyer, D. Wagner, C. Schubert, E. M. Pfeiffer, and C. Knoblauch. 2011. Methane oxidation associated with submerged brown mosses reduces methane emissions from Siberian polygonal tundra. *J. Ecol.* **99**: 914–922. doi:10.1111/j.1365-2745.2011.01823.x
- MacIntyre, S., A. T. Crowe, A. Cortés, and L. Arneborg. 2018. Turbulence in a small arctic pond. *Limnol. Oceanogr.* **63**: 2337–2358. doi:10.1002/lno.10941
- Mann, P. J., T. I. Eglinton, C. P. MacIntyre, N. Zimov, A. Davydova, J. E. Vonk, R. M. Holmes, and R. G. M. Spencer. 2015. Utilization of ancient permafrost carbon in headwaters of Arctic fluvial networks. *Nat. Commun.* **6**: 7856. doi:10.1038/ncomms8856
- Matveev, A., I. Laurion, B. N. Deshpande, N. Bhiry, and W. F. Vincent. 2016. High methane emissions from thermokarst lakes in subarctic peatlands. *Limnol. Oceanogr.* **61**: 5150–5164. doi:10.1002/lno.10311
- Matveev, A., I. Laurion, and W. F. Vincent. 2019. Winter accumulation of methane and its variable timing of release from thermokarst lakes in subarctic peatlands. *J. Geophys. Res. Biogeosci.* **124**: 3521–3535. doi:10.1029/2019JG005078
- McGinnis, D. F., J. Greinert, Y. Artemov, S. E. Beaubien, and A. Wüest. 2006. Fate of rising methane bubbles in stratified waters: How much methane reaches the atmosphere? *J. Geophys. Res.* **111**: C09007. doi:10.1029/2005JC003183
- Minke, M., N. Donner, N. S. Karpov, P. de Klerk, and H. Joosten. 2007. Distribution, diversity, development and dynamics of polygon mires: examples from Northeast Yakutia (Siberia). *Peatlands International* **1**: 36–40.
- Muster, S., and others. 2017. PeRL: A circum-Arctic Permafrost region pond and lake database. *Earth Syst. Sci. Data* **9**: 317–348. doi:10.5194/essd-9-317-2017
- Negandhi, K., I. Laurion, M. J. Whiticar, P. E. Galand, X. Xu, and C. Lovejoy. 2013. Small thaw ponds: An unaccounted source of methane in the Canadian High Arctic. *PloS One* **8**: e78204. doi:10.1371/journal.pone.0078204
- Negandhi, K., I. Laurion, and C. Lovejoy. 2014. Bacterial communities and greenhouse gas emissions of shallow ponds in the High Arctic. *Polar Biol.* **37**: 1669–1683. doi:10.1007/s00300-014-1555-1
- Nisbet, E. G., and others. 2019. Very strong atmospheric methane growth in the 4 years 2014–2017: Implications for the Paris Agreement. *Global Biogeochem. Cycles* **33**: 318–342. doi:10.1029/2018GB006009
- Olefeldt, D., M. R. Turetsky, P. M. Crill, and A. D. McGuire. 2013. Environmental and physical controls on northern terrestrial methane emissions across permafrost zones. *Glob. Change Biol.* **19**: 589–603. doi:10.1111/gcb.12071
- Pack, M. A., X. Xu, M. Lupascu, J. D. Kessler, and C. I. Czimczik. 2015. A rapid method for preparing low volume CH<sub>4</sub> and CO<sub>2</sub> gas samples for <sup>14</sup>C AMS analysis. *Org. Geochem.* **78**: 89–98. doi:10.1016/j.orggeochem.2014.10.010
- Pataki, D. E., and others. 2003. The application and interpretation of Keeling plots in terrestrial carbon cycle research. *Glob. Biogeochem. Cycles* **17**(1). doi:10.1029/2001GB001850
- Polishchuk, Y. M., A. N. Bogdanov, I. N. Muratov, V. Y. Polishchuk, A. Lim, R. M. Manasyrov, L. S. Shirokova, and

- O. S. Pokrovsky. 2018. Minor contribution of small thaw ponds to the pools of carbon and methane in the inland waters of the permafrost-affected part of the Western Siberian Lowland. *Environ. Res. Lett.* **13**: 045002. doi:[10.1088/1748-9326/aab046](https://doi.org/10.1088/1748-9326/aab046)
- Pienitz, R., P. T. Doran, and S. F. Lamoureux. 2008. Origin and geomorphology of lakes in the Polar regions, p. 25–41. *In* W. F. Vincent and J. Laybourn-Parry [eds.], *Polar lakes and rivers—limnology of arctic and antarctic aquatic ecosystems*. Oxford University.
- Prėskienis, V., I. Laurion, F. Bouchard, P. Douglas, M. F. Billett, D. Fortier, and X. Xu. 2020. Concentrations, fluxes and isotopic signatures of greenhouse gases emitted from lakes and ponds on Bylot Island, Nunavut, Canada. *Nordicana D collection at the Centre for northern studies (CEN)*, doi:[10.5885/45615XX-1A0AFEFB748D4457](https://doi.org/10.5885/45615XX-1A0AFEFB748D4457)
- Schuur, E. A. G., and others. 2015. Climate change and the permafrost carbon feedback. *Nature* **520**: 171–179. doi:[10.1038/nature14338](https://doi.org/10.1038/nature14338)
- Sebacher, D., R. C. Harriss, K. B. Bartlett, S. M. Sebacher, and S. S. Grice. 1986. Atmospheric methane sources: Alaskan tundra bogs, and alpine fen, and a subarctic boreal marsh. *Tellus* **38B**: 1–10. doi:[10.3402/tellusb.v38i1.15059](https://doi.org/10.3402/tellusb.v38i1.15059)
- Sepulveda-Jauregui, A., K. M. Walter Anthony, K. Martinez-Cruz, S. Greene, and F. Thalasso. 2015. Methane and carbon dioxide emissions from 40 lakes along a north–south latitudinal transect in Alaska. *Biogeosciences* **12**: 3197–3223. doi:[10.5194/bg-12-3197-2015](https://doi.org/10.5194/bg-12-3197-2015)
- Sturtevant, C. S., and W. C. Oechel. 2013. Spatial variation in landscape-level CO<sub>2</sub> and CH<sub>4</sub> fluxes from arctic coastal tundra: influence from vegetation, wetness, and the thaw lake cycle. *Glob. Change Biol.* **19**: 2853–2866. doi:[10.1111/gcb.12247](https://doi.org/10.1111/gcb.12247)
- Tan, Z., and Q. Zhuang. 2015. Arctic lakes are continuous methane sources to the atmosphere under warming conditions. *Environ. Res. Lett.* **10**: 054016. doi:[10.1088/1748-9326/10/5/054016](https://doi.org/10.1088/1748-9326/10/5/054016)
- Tan, Z., Q. Zhuang, N. J. Shurpali, M. E. Marushchak, C. Biasi, W. Eugster, and K. Walter Anthony. 2017. Modeling CO<sub>2</sub> emissions from Arctic lakes: Model development and site-level study. *J. Adv. Model. Earth Syst.* **9**: 2190–2213. doi:[10.1002/2017MS001028](https://doi.org/10.1002/2017MS001028)
- Tank, S. E., J. E. Vonk, M. A. Walvoord, J. W. McClelland, I. Laurion, and B. W. Abbott. 2020. Landscape matters: Predicting the biogeochemical effects of permafrost thaw on aquatic networks with a state of factor approach. *Permafr. Periglac. Process.* **31**: 358–370. doi:[10.1002/ppp.2057](https://doi.org/10.1002/ppp.2057)
- Thanh-Duc, N., P. Crill, and D. Bastviken. 2010. Implications of temperature and sediment characteristics on methane formation and oxidation in lake sediments. *Biogeochemistry* **100**: 185–196. doi:[10.1007/s10533-010-9415-8](https://doi.org/10.1007/s10533-010-9415-8)
- Thottathil, S. D., P. C. J. Reis, R. A. del Giorgio, and Y. T. Prairie. 2018. The extent and regulation of summer methane oxidation in northern lakes. *Eur. J. Vasc. Endovasc. Surg.* **123**: 3216–3230. doi:[10.1029/2018JG004464](https://doi.org/10.1029/2018JG004464)
- Treat, C. C., and M. C. Jones. 2018. Near-surface permafrost aggradation in Northern Hemisphere peatlands shows regional and global trends during the past 6000 years. *Holocene* **28**: 998–1010. doi:[10.1177/0959683617752858](https://doi.org/10.1177/0959683617752858)
- Turetsky, M. R., and others. 2020. Carbon release through abrupt permafrost thaw. *Nat. Geosci.* **13**: 138–143. doi:[10.1038/s41561-019-0526-0](https://doi.org/10.1038/s41561-019-0526-0)
- Vachon, D., and Y. T. Prairie. 2013. The ecosystem size and shape dependence of gas transfer velocity versus wind speed relationships in lakes. *Can. J. Fish. Aquat. Sci.* **70**: 1757–1764. doi:[10.1139/cjfas-2013-0241](https://doi.org/10.1139/cjfas-2013-0241)
- Vézina, S., and W. F. Vincent. 1997. Arctic cyanobacteria and limnological properties of their environment: Bylot Island, Northwestern Territories, Canada (73°N, 80°W). *Polar Biol.* **17**: 523–534. doi:[10.1007/s003000050151](https://doi.org/10.1007/s003000050151)
- Walter Anthony, K. M., and S. MacIntyre. 2016. Nocturnal escape route for marsh gas. *Nature* **535**: 363–365. doi:[10.1038/535363a](https://doi.org/10.1038/535363a)
- Walter Anthony, K. M., D. A. Vas, L. Brosius, F. S. Chapin, S. A. Zimov, and Q. L. Zhuang. 2010. Estimating methane emissions from northern lakes using ice-bubble surveys. *Limnol. Oceanogr. Methods* **8**: 592–609. doi:[10.4319/lom.2010.8.0592](https://doi.org/10.4319/lom.2010.8.0592)
- Walter Anthony, K. M., R. Daanen, P. Anthony, T. Schneider von Deimling, C. L. Ping, J. P. Chanton, and G. Grosse. 2016. Methane emissions proportional to permafrost carbon thawed in Arctic lakes since the 1950s. *Nat. Geosci.* **22**: 679–682. doi:[10.1038/NGEO2795](https://doi.org/10.1038/NGEO2795)
- Walter, K. M., S. A. Zimov, J. P. Chanton, D. Verbyla, and F. S. Chapin. 2006. Methane bubbling from Siberian thaw lakes as a positive feedback to climate warming. *Nature* **443**: 71–75. doi:[10.1038/nature05040](https://doi.org/10.1038/nature05040)
- Walter, K. M., J. P. Chanton, F. S. Chapin, E. A. G. Schuur, and S. A. Zimov. 2008. Methane production and bubble emissions from arctic lakes: Isotopic implications for source pathways and ages. *J. Geophys. Res.* **113**. doi:[10.1029/2007JG000569](https://doi.org/10.1029/2007JG000569)
- Wanninkhof, R. 1992. Relationship between wind-speed and gas exchange over the ocean. *J. Geophys. Res. Oceans* **97**: 7373–7382. doi:[10.1029/92jc00188](https://doi.org/10.1029/92jc00188)
- West, W. E., S. M. McCarthy, and S. E. Jones. 2015. Phytoplankton lipid content influences freshwater lake methanogenesis. *Freshwater Biol.* **60**: 2261–2269. doi:[10.1111/fwb.12652](https://doi.org/10.1111/fwb.12652)
- Whiticar, M. J., E. Faber, and M. Schoell. 1986. Biogenic methane formation in marine and freshwater environments: CO<sub>2</sub> reduction vs. acetate fermentation—Isotope evidence. *Geochim. Cosmochim. Acta* **50**: 693–709. doi:[10.1016/0016-7037\(86\)90346-7](https://doi.org/10.1016/0016-7037(86)90346-7)
- Wik, M., P. M. Crill, R. K. Varner, and D. T. Bastviken. 2013. Multiyear measurements of ebullitive methane flux from three subarctic lakes. *J. Geophys. Res. Biogeosci.* **118**: 1307–1321. doi:[10.1002/jgrg.20103](https://doi.org/10.1002/jgrg.20103)

- Wik, M., B. F. Thornton, D. T. Bastviken, S. MacIntyre, R. K. Varner, and P. M. Crill. 2014. Energy input is the primary controller of methane bubbling in subarctic lakes. *Geophys. Res. Lett.* **41**: 555–560. doi:[10.1002/2013GL058510](https://doi.org/10.1002/2013GL058510)
- Wik, M., R. K. Varner, K. Walter Anthony, S. MacIntyre, and D. T. Bastviken. 2016a. Climate-sensitive northern lakes and ponds are critical components of methane release. *Nat. Geosci.* **9**: 99–105. doi:[10.1038/NGEO2578](https://doi.org/10.1038/NGEO2578)
- Wik, M., B. F. Thornton, D. T. Bastviken, J. Snöälvi, and P. Crill. 2016b. Biased sampling of methane release from northern lakes: A problem for extrapolation. *Geophys. Res. Lett.* **43**: 1256–1262. doi:[10.1002/2015GL066501](https://doi.org/10.1002/2015GL066501)
- Woolway, R. I., and C. J. Merchant. 2019. Worldwide alteration of lake mixing regimes in response to climate change. *Nat. Geosci.* **12**: 271–276. doi:[10.1038/s41561-019-0322-x](https://doi.org/10.1038/s41561-019-0322-x)
- Yvon-Durocher, G., A. P. Allen, D. T. Bastviken, R. Conrad, C. Gudas, A. St-Pierre, N. Thanh-Duc, and P. A. del Giorgio. 2014. Methane fluxes show consistent temperature dependence across microbial to ecosystem scales. *Nature* **507**: 488–493. doi:[10.1038/nature13164](https://doi.org/10.1038/nature13164)
- Zimov, S. A., and others. 1997. North Siberian lakes: A methane source fueled by Pleistocene carbon. *Science* **277**: 800–802. doi:[10.1126/science.277.5327.800](https://doi.org/10.1126/science.277.5327.800)

## Acknowledgments

We are grateful to Parks Canada, the Centre for Northern Studies (CEN) and G. Gauthier for helping with logistics during fieldwork, A. Veillette, M. Tremblay, Y. Seyer, T. Pacoureaux and F. Mazoyer for their assistance with collecting and processing of the samples, M. Bartosiewicz and S. MacIntyre for advice on data analyses, and S. Duval and T. Hao Bui for gas chromatography and stable isotope analyses. The study was funded by the Natural Sciences and Engineering Research Council Discovery program, Network of Centres of Excellence ArcticNet, Natural Resources Canada Polar Continental Shelf Program, International Polar Year, and Fonds de recherche du Québec—Nature et technologies team grant (IL), as well as the CREATE program EnviroNorth (VP) and the W. Garfield Weston Foundation (FB). We also thank the NERC Radiocarbon Facility and M. Garnett for supporting and contributing to <sup>14</sup>C analysis through allocations 1857.1014 and 1995.0416.

## Conflict of interest

None declared.

Submitted 13 November 2019

Revised 28 June 2020

Accepted 18 November 2020

Associate editor: Suzanne E. Tank